Diagnosis of turbulent fluxes in the grey zone from large-eddy simulations of convective boundary layers

Amber Nusteling

Dept. of Geosciences and Remote Sensing and Faculty CEG
Delft University of Technology
Supervisor: Dr. S. R. de Roode
Second examiner: Prof.dr. A. P. Siebesma
Third examiner: Prof.dr. D. J. E. M. Roekaerts

8 July 2019

Abstract

Turbulent transport is present on a range of scales from a few times the height of the boundary layer to the Kolmogorov scale. Numerical weather prediction (NWP) models are not able to resolve any turbulence that is present at scales smaller than their horizontal grid size, so they parametrise it entirely. Advances in computational power allow NWP models to move to finer resolutions. Below resolutions of about 10 km, they enter the 'grey zone', where part of the turbulent scales can be resolved. The remaining subgrid-scale turbulent fluxes still need to be parametrised. In this study, the scale dependency of these subgrid-scale turbulent fluxes is diagnosed for NWP models that operate at grey zone resolutions. Special attention is paid to the horizontal subgrid fluxes. Furthermore, the validity of a possible parametrisation on the basis of an eddy diffusivity is discussed. The DALES Large Eddy Simulation (LES) model is used to diagnose the turbulence and to provide a three-dimensional field with a high resolution. Two cases are considered: a convective boundary layer (CBL) in which the buoyancy flux has strong contribution from the moisture flux and a CBL with strong wind shear and subsidence. The LES fields are coarse-grained to represent NWP models of different grid sizes. The subgrid-scale turbulent fluxes that would be parametrised in the NWP model, can be diagnosed from the coarse-grained field. This approach proves to be a valuable diagnostic tool for vertical subgrid fluxes. Flux partitioning shows that the subgrid contribution to turbulence starts dominating over the resolved part above scales of about 1 km, in good agreement with the literature. The grid size at which subgrid contribution becomes larger than the resolved is slightly different for the structures of temperature and humidity, suggesting those scalars should be parameterised separately. Horizontal subgrid fluxes start dominating over the resolved fluxes at the same scale as for the vertical fluxes, beyond 1 km resolutions. The horizontal subgrid fluxes are of about the same magnitude as the vertical fluxes in the entrainment zone, whereas they are two orders of magnitude smaller in the middle of the boundary layer. Although the horizontal fluxes are smaller in comparison to the vertical fluxes, they are not negligible. Overall, the magnitude of the horizontal subgrid fluxes increases with grid size, just like the magnitude of the vertical fluxes. This effect is even more evident in the simulation case with a strong wind shear, because the momentum flux is drastically increased. If the magnitude of the horizontal subgrid fluxes does not decline for large grid sizes, it is not justified to neglect horizontal fluxes entirely at those large grid sizes. The contribution of the subgrid transport to the tendency of the mean quantities in the NWP model is indicated by the flux divergence. Because of periodic boundary conditions, the slab-averaged flux divergences are zero. So, to estimate the magnitude of the flux divergences the width of the probability density function is used. It is found that the vertical and horizontal transport contribute similarly to the tendency of the mean for grid sizes at grey zone resolutions. Horizontal transport cannot be neglected in the grey zone, as it is at NWP grid sizes above 10 km. Finally, the eddy diffusivity for the vertical and horizontal direction were compared. The eddy diffusivity for the vertical direction increases with grid size in the grey zone, and ultimately reaches an asymptotic value for a grid size of 3.2 km. This behaviour is in agreement with the literature, which also shows that the eddy diffusivity saturates for a certain grid size. The behaviour of the eddy diffusivity for the horizontal direction does not resemble the behaviour for the vertical direction. This anisotropy suggests that the eddy diffusivity has to be defined separately for each direction.

Contents

Abstract **1**

Contents **2**

1 Introduction **3**

2 Theory **5**
2.1 DALES 5
2.2 Subfilter-scale models 5
2.3 Length scales 6
2.4 Subgrid parametrisation in coarse-grained grids 7

3 Experimental Method **8**
3.1 A diagnosis of budget equations at NWP scales from high-resolution LES fields 8
3.2 Interpolation of LES fields to full and half levels 13
3.3 Definition of the coarse-graining process 13
3.4 Consequences of coarse-graining budget equations 15
3.5 Direct diagnosis of the flux divergence from LES fields 16
3.6 Down-gradient diffusion model 18
3.7 Simulation cases 19

4 Results and Discussion **22**
4.1 Vertical flux behaviour 22
4.2 Horizontal flux behaviour 29
4.2.1 Height dependency of slab-averaged horizontal fluxes 29
4.2.2 Scale dependency of horizontal subgrid fluxes 30
4.2.3 Comparison of flux divergences and their calculation methods 36
4.3 K-diffusion analysis 38

5 Conclusion **40**

References **42**

Appendix **43**

1 Introduction

The scale of turbulent transport ranges from the largest eddy sizes at the scale of the boundary layer to the smallest eddy sizes where the turbulent kinetic energy is dissipated. In the past, numerical weather prediction (NWP) models did not have a fine enough resolution to resolve turbulence. However, turbulence is an important mechanism for the distribution of heat, moisture and momentum, so it needs to be parametrised. The ever-increasing computational power has made it possible to keep refining the resolution of NWP models. Regional weather forecast models currently use grid sizes down to 1 km. Below a 10 km resolution these weather models can resolve a fraction of the turbulent transport, but not all of it. This region, below 10 km resolutions, is called the 'terra incognita' or 'grey zone' (Wyngaard (2004)). The remaining unresolved turbulent fluxes need to be parametrised. Previously, Honnert et al. (2011) and Shin and Hong (2013) used high-resolution modelling data to diagnose the dependency of the resolved flux on the applied horizontal grid size.

Although the parametrisation of subgrid horizontal fluxes is commonly applied in turbulence-resolving atmospheric models, almost no attention has been paid to the scale dependency of horizontal fluxes at grey zone solutions. The aim of this thesis project is to better understand how to capture the scale dependency of subgrid fluxes needed in parametrisations for NWP models that operate at grey zone resolutions. To this end we will use three-dimensional fields obtained from the high-resolution turbulence-resolving DALES Large Eddy Simulation (LES) model. The latter model solves the conservation equations of heat, momentum and moisture at spatial resolutions that are typically in the range of 3 to 100 m. Two different simulation cases are run in the DALES model. The buoyancy-driven convective boundary layer (CBL) simulation case as in De Roode et al. (2004) is used as well as a CBL case with a high wind speed and subsidence. A coarse-graining approach based on Honnert et al. (2011) is used to diagnose the fluxes of temperature or humidity for grids of different sizes from the information from the LES model. In addition, the horizontal flux divergence is even more directly connected to how the horizontal subgrid transport impacts the tendency of the mean in NWP models. The flux divergences will be investigated for different grid sizes at grey zone resolutions.

Kurowski and Teixeira (2018) stretched their LES grid sizes to match NWP scales, in order to find vertical and horizontal subgrid heat fluxes in a dry convective boundary layer from their LES parametrisation. They found that the vertical subgrid heat fluxes increase steadily for larger NWP grid sizes. Around a grid size of 10 km its asymptotic value is reached. Conversely, horizontal heat fluxes decrease slightly and then rapidly for increasing grid sizes. Because we coarse-grain the original LES fields instead of using a parametrisation, it will be interesting to see how the results compare for our approach.

In addition to the diagnosis of the fluxes, it will be attempted to construct a parametrisation for the horizontal fluxes. A parametrisation on the basis of K-theory makes sense, because a similar scheme is also used for subgrid fluxes in large eddy simulation models. Moreover, Boutle et al. (2014) already use K-theory in their parametrisation for NWP models. They have parametrised the subgrid fluxes using a Smagorinsky model that solves the steady-state subgrid TKE equation using a down-gradient diffusion approach for the buoyancy flux and wind shear production term. The total turbulent fluxes depend partly on this parametrisation, and the contribution from the latter depends delicately on the applied mesh size. Also, Simon et al. (2019) have assessed the grid dependency of four LES turbulence models, the Smagorinsky model, a turbulent kinetic energy order-1.5 (TKE-1.5) model, and two dynamic reconstruction models, using simulation data at resolutions from 25 m to 1 km. They found that the first two models, based on defining an eddy diffusivity, did not perform well for coarse resolutions. With our coarse-grained results, we will be able to diagnose the scale dependency of the eddy diffusivity K. In DALES, isotropic diffusion is used (Heus et al., 2010). It will be evaluated whether this is a valid assumption if the horizontal grid resolution becomes much larger than the vertical grid resolution, as is the case in NWPs. When the diffusion is anisotropic, separate values of the eddy diffusivity K have to be found for the horizontal and vertical direction.

In the following, a theoretical background of DALES and the subfilter-scale models will be given. The coarse-graining approach and method of flux diagnosis will be outlined as well as the simulation cases used in the study. The methods of parametrisation using K-diffusion will also be explained. Finally, the results for the vertical fluxes, horizontal fluxes and K-diffusion approach will be discussed.

2 Theory

2.1 DALES

DALES resolves turbulent scales larger than a certain filter size, and uses a parametrisation for the smaller scales. Global weather forecast models cannot resolve turbulence, because their grid sizes are above 10 km. Regional weather models can reach a resolution of 1 km, but only resolve part of the turbulence and need a parametrisation for the remaining part. Direct Numerical Simulation (DNS) solves turbulence up to the Kolmogorov scales which is why it does not require a subgrid model. However, DNS covers a domain of a few metres across and is only able to handle low Reynolds number flows. DNS is not suitable to study atmospheric flows with convective clouds, since convective clouds have scales up to a few km. For the purpose of this research LES is the most suitable tool, because it can give a reasonably detailed field of the velocities, temperature and moisture, as well as span multiple square kilometres of area. This makes it possible to do a study in the grey zone of NWP.

The key variables used in DALES are the three velocity components u_i, the liquid water potential temperature θ, the total, water vapour and cloud liquid water specific humidity q_t, q_v and q_l, the subfilter-scale turbulent kinetic energy e and scalars like rain or chemical species.

DALES simulates the atmosphere over time by using filtered fluid dynamics equations. This makes it possible to resolve the scales greater than the filter length, while accounting for the subgrid fluxes. Eq. (1) is the continuity equation (conservation of mass). Eq. (2) is the momentum equation including buoyancy and the Coriolis force. Finally, Eq. (3) accounts for the time dependency of a certain scalar quantity ϕ, for example the liquid water potential temperature or the specific humidity. The tildes denote a filtered variable. For large Reynolds number flows, typical for the atmosphere, viscous transport terms can be neglected.

$$\frac{\partial \tilde{u}_i}{\partial x_i} = 0 \tag{1}$$

$$\frac{\partial \tilde{u}_i}{\partial t} = -\frac{\partial \tilde{u}_i \tilde{u}_j}{\partial x_j} - \frac{\partial \pi}{\partial x_i} + \frac{g}{\theta_0}\tilde{\theta}_\mathrm{v}\delta_{i3} + F_i - \frac{\partial \tau_{ij}}{\partial x_j} \tag{2}$$

$$\frac{\partial \tilde{\phi}}{\partial t} = -\frac{\partial \tilde{u}_j \tilde{\phi}}{\partial x_j} - \frac{\partial R_{u_j,\phi}}{\partial x_j} + S_\phi \tag{3}$$

Here, $\pi = \frac{\tilde{p}}{\rho_0} + \frac{2}{3}e$ is the modified pressure, δ_{ij} is the Kronecker delta, F_i includes other forcings, such as the Coriolis acceleration, and $\tau_{ij} = \widetilde{u_i u_j} - \tilde{u_i}\tilde{u_j} + \frac{2}{3}e$ is the deviatoric part of the subgrid momentum flux. The virtual potential temperature θ_v is related to the potential temperature θ and total humidity q_t as,

$$\theta_\mathrm{v} = \theta(1 + (\frac{R_v}{R_d} - 1)q_\mathrm{t}), \tag{4}$$

in the absence of clouds (De Roode et al., 2004). R_v and R_d are the specific gas constants for water vapour and dry air, respectively. The factor $\frac{R_v}{R_d} - 1$ is often approximated to 0.61. S_ϕ denotes the source terms, such as radiative terms, and $R_{uj,\phi}$ are the subfilter-scale scalar fluxes (Heus et al., 2010).

2.2 Subfilter-scale models

In the filtered DALES equations above, momentum flux τ_{ij} and and scalar flux $R_{u_j,\phi}$, have to be parametrised. According to Deardorff (1980) τ_{ij} and $R_{u_j,\phi}$ can be given as

$$\tau_{ij} = \widetilde{u_i u_j} - \tilde{u_i}\tilde{u_j} - \frac{2}{3}\delta_{ij}\tilde{e} = -K_m\left(\frac{\partial \tilde{u_j}}{\partial x_i} + \frac{\partial \tilde{u_i}}{\partial x_j}\right), \tag{5}$$

$$R_{u_j,\phi} = \widetilde{u_j'' \phi''} = -K_h \frac{\partial \tilde{\phi}}{\partial x_j}. \tag{6}$$

The $\frac{2}{3}\delta_{ij}\tilde{e}$ term is compensated by the extra term in the modified pressure. K_m is the eddy viscosity for momentum and K_h is the eddy diffusivity for scalars. Both coefficients can be taken proportional to the subfilter-scale TKE e,

$$K_m = c_m l\sqrt{\tilde{e}} \tag{7}$$

$$K_h = c_h l\sqrt{\tilde{e}}. \tag{8}$$

Here, l is the characteristic length scale of the subfilter-scale eddies and c_m and c_h are the proportionality constants for momentum and scalar contributions, respectively. In DALES, the geometric mean of the grid sizes Δx, Δy and Δz is used as a length scale l_Δ, as introduced by Deardorff (1973),

$$l_\Delta = \left(\Delta x \Delta y \Delta z\right)^{1/3}. \tag{9}$$

2.3 Length scales

Several models for the length scale l have been proposed, that are different from l_Δ in Eq. (9). The notation for the different length scales was taken from De Roode et al. (2017). Firstly, Deardorff (1980) modifies the length scale l_Δ, to account for a situation where l is much smaller than the grid size. This happens for example in stably stratified regions. A measure for vertical atmospheric stability is the Brunt-Väisälä frequency N. It expresses the angular frequency at which an air parcel will oscillate when it is vertically displaced. N is given by

$$N = \left(\frac{g}{\theta_0}\frac{\partial \theta_\mathrm{v}}{\partial z}\right)^{1/2}. \tag{10}$$

In a neutral atmosphere, $N^2 = 0$, and by extension $\frac{\partial \theta_\mathrm{v}}{\partial z} = 0$. In such an atmosphere, an air parcel will not move. If $N^2 > 0$ (or $\frac{\partial \theta_\mathrm{v}}{\partial z} > 0$), a vertically displaced air parcel will start oscillating around its original position. This atmosphere is called stable. Lastly, if $N^2 < 0$ (or $\frac{\partial \theta_\mathrm{v}}{\partial z} < 0$), the atmosphere is convective. In this case the air parcel will be accelerated away from its original position (Nieuwstadt et al., 2016). In the context of length scales, the Brunt-Väisälä frequency can be used to construct a stability-dependent length scale l_D,

$$l_D = c_n \frac{e^{1/2}}{N}. \tag{11}$$

The mixing length l is equal to l_D when $l < l_\Delta$. Deardorff (1980) takes $l = \Delta x$ for $l \geq l_\Delta$, whereas De Roode et al. (2017) uses $l = l_\Delta$. There is a third length scale l_M that Mason and Thomson (1992) proposed. When we take $n = 2$ as suggested by Brown et al. (1994), l_M is given by

$$\frac{1}{l_M^2} = \frac{1}{\left(\kappa(z+z_0)\right)^2} + \frac{1}{\left(c_s l_\Delta\right)^2}. \tag{12}$$

Here, κ is the von Kármán constant, z_0 is the roughness length and c_s is the Smagorinsky constant. The length scale l_M applies the stability-dependence of the region near the surface throughout the rest of the flow. The length scales $c_s l_\Delta$ in the flow interior and $\kappa(z+z_0)$ near the surface are blended. Boutle et al. (2014) used $z_0 = 0$ and proceeded to incorporate l_M into a blended mixing length l_{blend} of a 1D boundary layer scheme and a 3D Smagorinsky scheme,

$$l_{blend} = W_{1D} l_{bl} + (1 - W_{1D}) l_M. \tag{13}$$

The function W_{1D} gives a measure of the resolved turbulence ($W_{1D} = 1$ when the turbulence is unresolved, $W_{1D} = 0$ when resolved). The length scale l_{bl} holds for the 1D boundary layer scheme.

2.4 Subgrid parametrisation in coarse-grained grids

In our study, the subfilter parametrisation specified for DALES in Eqs. (5) to (8) will be applied to coarse-grained grids that represent NWP grids at grey zone resolutions. Like in DALES, the subgrid momentum and scalar fluxes in an NWP model are given by subgrid parametrisations. The subgrid fluxes of the NWP model are diagnosed from high-resolution LES fields. The subgrid fluxes in each LES grid box are not taken into account when determining the NWP subgrid fluxes, because they are small everywhere except at the surface (see Fig. 9). Furthermore, we determine the eddy diffusivity K_h for the NWP subgrid fluxes in our analysis. To obtain the constant c_h in Eq. (8), $l = \Delta x$ is used for simplicity. Because the NWP subgrid fluxes and eddy diffusivity are investigated, Δx is equal to the grid size of the NWP model. In this report we only show K, so l was not used explicitly.

3 Experimental Method

3.1 A diagnosis of budget equations at NWP scales from high-resolution LES fields

In this research, fields from LES simulations are used to probe characteristics of grey zone NWP models. The subgrid fluxes in a NWP grid box $\langle u_i'' \phi'' \rangle$ as well as the subgrid flux divergences $\frac{\partial \langle u_i'' \phi'' \rangle}{\partial x_i}$ are important to diagnose, because they appear in the governing equation in NWP models that is needed to calculate changes in velocities and scalars over time (Eq. (14)),

$$\frac{\partial \langle \phi \rangle}{\partial t} = -\langle u_i \rangle \frac{\partial \langle \phi \rangle}{\partial x_i} - \frac{\partial \langle u_i'' \phi'' \rangle}{\partial x_i} + \langle S_\phi \rangle. \tag{14}$$

The double primes indicate a fluctuation of a quantity relative to the NWP grid box value. The angular brackets $\langle . \rangle$ signify an averaging over an NWP grid box. The change in time of the grid box mean value of the quantity ϕ is dictated by the resolved transport $-\langle u_i \rangle \frac{\partial \langle \phi \rangle}{\partial x_i}$ and the subgrid transport $-\frac{\partial \langle u_i'' \phi'' \rangle}{\partial x_i}$. We only focus on transport here, additional forcings are denoted by $\langle S_\phi \rangle$. For the subgrid transport $-\frac{\partial \langle u_i'' \phi'' \rangle}{\partial x_i}$, a parametrisation for $\langle u_i'' \phi'' \rangle$ is needed to close the equation. It is commonly assumed that fluxes $\langle u_i'' \phi'' \rangle$ can be represented by a down-gradient diffusion approach (see also Kurowski and Teixeira (2018)),

$$\langle u_i'' \phi'' \rangle = -K_\phi \frac{\partial \langle \phi \rangle}{\partial x_i}. \tag{15}$$

The goal of this research is to diagnose the subgrid fluxes and flux divergences, as well as assess whether the down-gradient diffusion parametrisation may be used in NWP models that operate at grey zone resolutions.

The procedure used to find the subgrid fluxes and flux divergences is described for a velocity u_i in the horizontal or vertical direction and a scalar ϕ, like θ, θ_v or q_t. The pixel plots that illustrate each step depict vertical velocity w and liquid potential temperature θ at a height of $z/z_i = 0.5$. Three-dimensional fields of u_i and ϕ are obtained from LES. An LES simulation has a domain size of $L_x \times L_y \times H$, where $L_x = L_y$ is the total domain width and H is the domain height. The grid consists of $N_x \times N_y \times k_{max}$ grid boxes with sizes $\Delta x_{LES} = 50$ m and $\Delta z = 20$ m. Δx_{LES} is the horizontal grid box width in both the x- and y-direction. At each LES grid box the three velocity components u_i, the liquid water potential temperature θ, the total, water vapour and cloud liquid water specific humidity q_t, q_v and q_l, the subfilter-scale turbulent kinetic energy e and scalars like rain or chemical species are known. LES fields of w and θ are shown as an example in the left columns of Figs. 2 and 3.

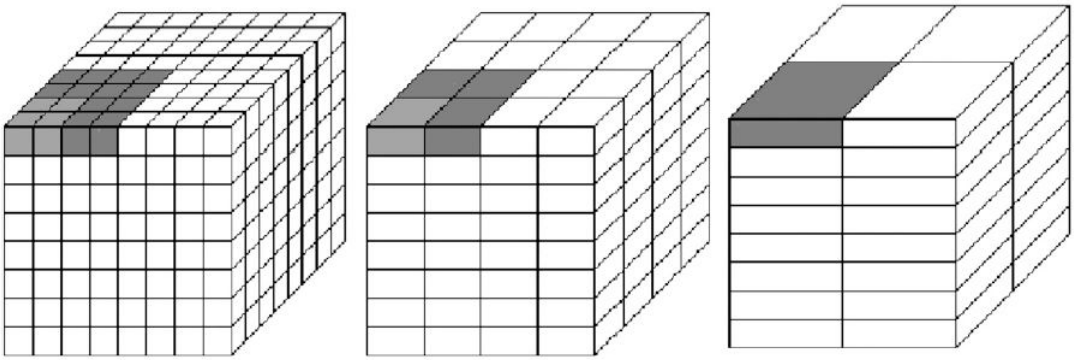

Figure 1: The coarse-graining process. On the left is the original LES mesh with grid width Δx_{LES}, in the middle the mesh is coarse-grained once with $\Delta x_{NWP} = 2\Delta x_{LES}$ and on the right the mesh is coarse-grained twice with $\Delta x_{NWP} = 4\Delta x_{LES}$. Image copied from Honnert et al. (2011).

To assess what a field would look like at an arbitrary grid size used by an NWP, denoted by Δx_{NWP}, the LES fields are subjected to coarse-graining. This entails averaging the values inside subdomains with width Δx_{NWP}, as illustrated in Fig. 1. The resulting values of u_i and ϕ in the new grid are denoted by $\langle u_i \rangle$ and $\langle \phi \rangle$. The coarse-graining process is detailed further in section 3.3.

The pixel plots that are obtained for $\langle w \rangle$ and $\langle \theta \rangle$ after the coarse-graining process are given in the middle column of Figs. 2 and 3. The same colours are assigned to the same values in the left and middle column. The coarse-grained plots represent what the measurement field from an NWP model with grid width Δx_{NWP} would look like. From top to bottom, the coarse-grained fields are given for $\Delta x_{NWP} = 0.2$ km, $\Delta x_{NWP} = 0.8$ km and $\Delta x_{NWP} = 6.4$ km. When the grid size becomes coarser, it can be clearly seen that less structures are resolved. Also, fluctuations are defined relative to the local average, as $u_i'' = u_i - \langle u_i \rangle$ and $\phi'' = \phi - \langle \phi \rangle$. In the right column of Figs. 2 and 3, the fluctuations w'' and θ'' are shown for the three different Δx_{NWP}. Because all plots in the right column use the same colour-coding, it is evident that fluctuations from the local average increase with larger Δx_{NWP}. Fluctuations are especially small at $\Delta x_{NWP} = 0.2$ km, showing that the fields of $\langle w \rangle$ and $\langle \theta \rangle$ retain most of the details from the w and θ fields. The differences between w and θ are also visible in the pixel plots. The structures of w are smaller in scale than those of θ. The result of this is, that at the same Δx_{NWP} more of the structure in θ is resolved than in w. At $\Delta x_{NWP} = 6.4$ km, $\langle w \rangle$ is almost zero everywhere, whereas $\langle \theta \rangle$ still has some structure.

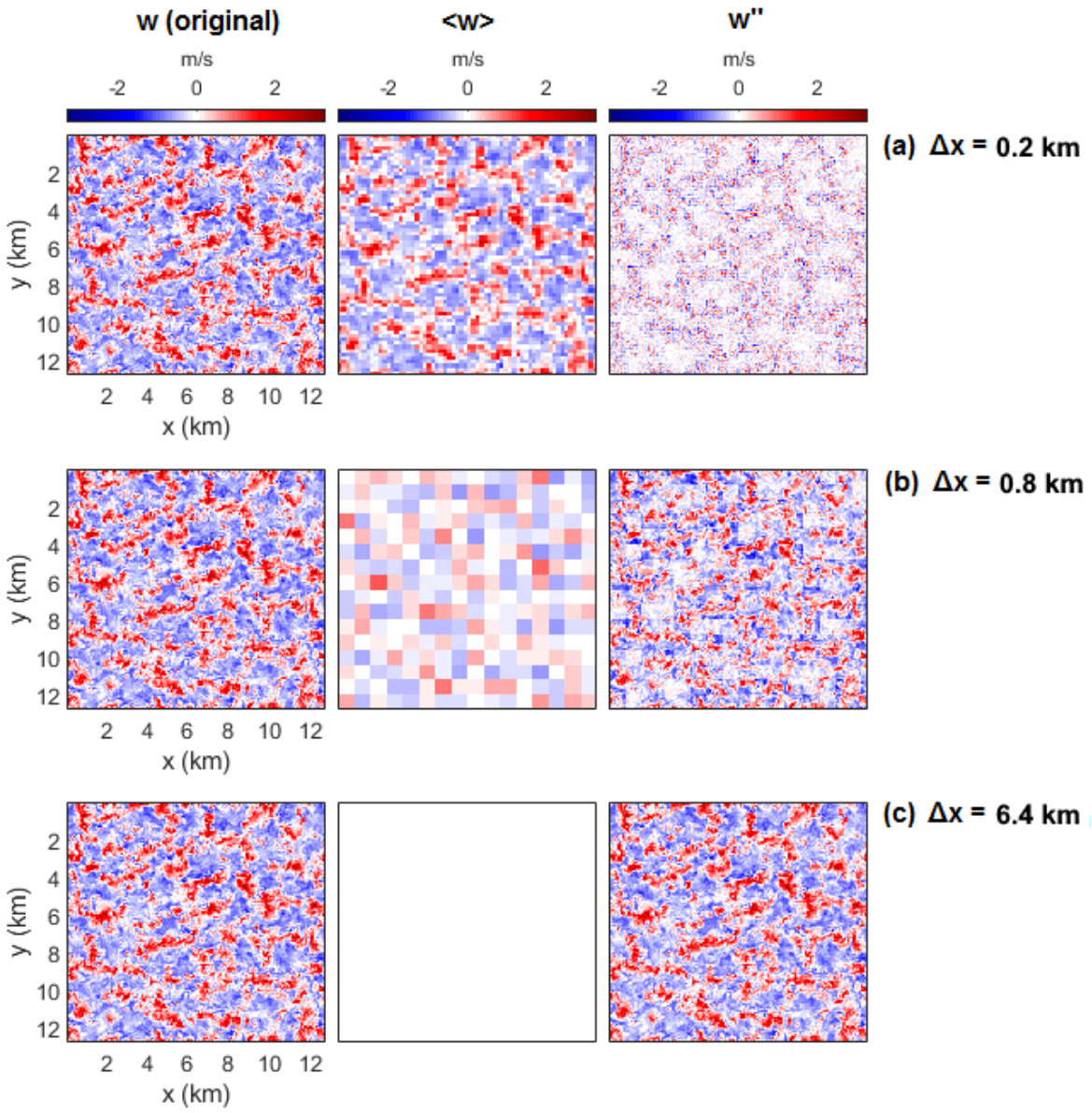

Figure 2: Examples of the original LES fields w (left column), the coarse-grained fields $\langle w \rangle$ (middle column) and the fluctuation field $w'' = w - \langle w \rangle$ (right column). The coarse-grained fields in the middle column could be considered as a fictitious horizontal mesh of an NWP, with mesh size $\Delta x_{NWP} = 0.2$ km for (a), $\Delta x_{NWP} = 0.8$ km for (b) and $\Delta x_{NWP} = 6.4$ km for (c).

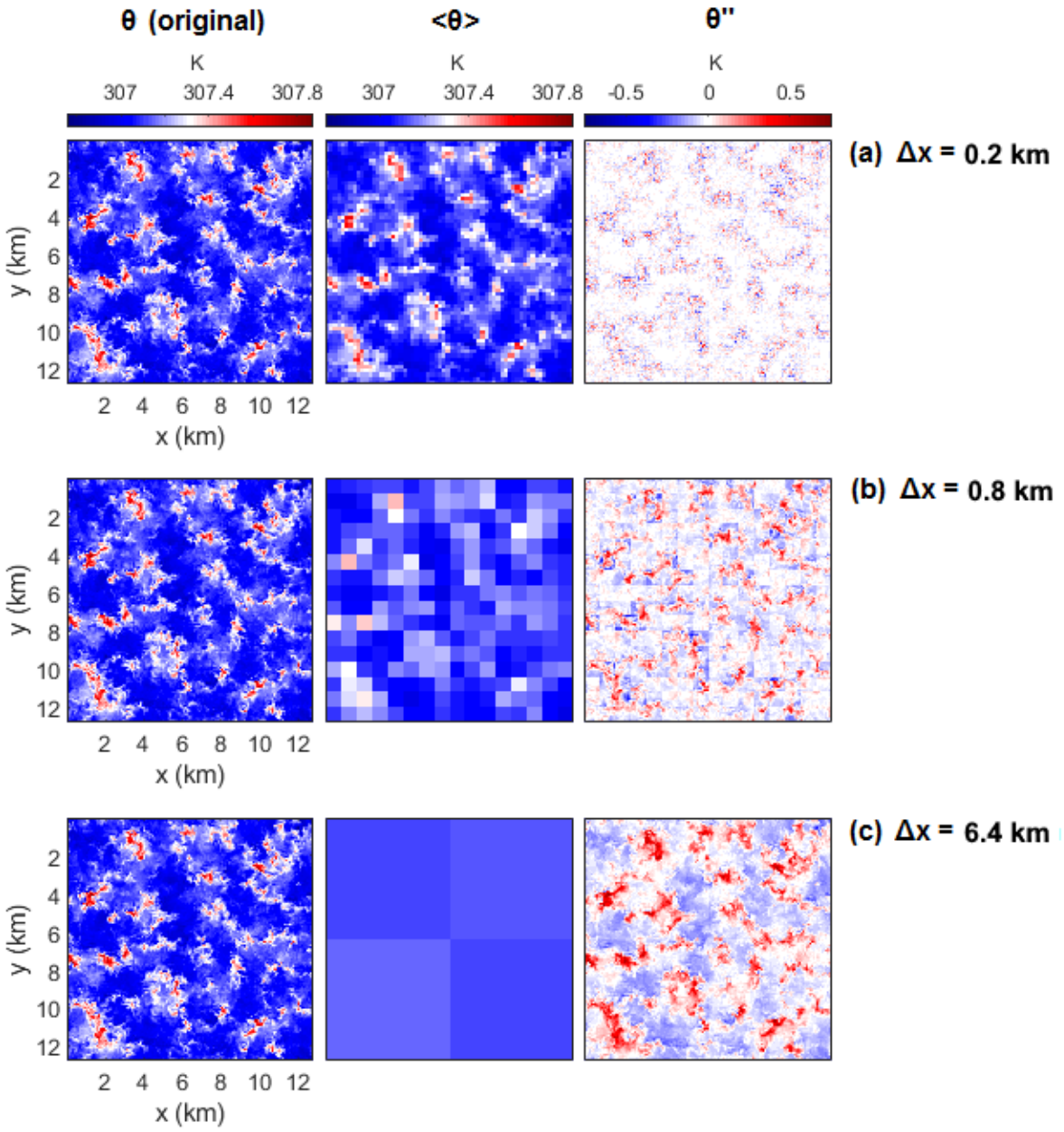

Figure 3: Examples of the original LES fields θ (left column), the coarse-grained fields $\langle\theta\rangle$ (middle column) and the fluctuation field $\theta'' = \theta - \langle\theta\rangle$ (right column). The coarse-grained fields in the middle column could be considered as a fictitious horizontal mesh of an NWP, with mesh size $\Delta x_{NWP} = 0.2$ km for (a), $\Delta x_{NWP} = 0.8$ km for (b) and $\Delta x_{NWP} = 6.4$ km for (c).

In the next step towards finding the subgrid fluxes, the fluctuations u_i'' and ϕ'' are multiplied to obtain $u_i''\phi''$. In the left column of Fig. 4 is depicted what this multiplication looks like for w and θ fields. The multiplication field can go through a similar coarse-graining process as the original LES fields, such that subgrid flux $\langle u_i''\phi''\rangle$ can be found. In the right column of Fig. 4, pixel plots are given for $\langle w''\theta''\rangle$. The same colours are used in the first and second column.

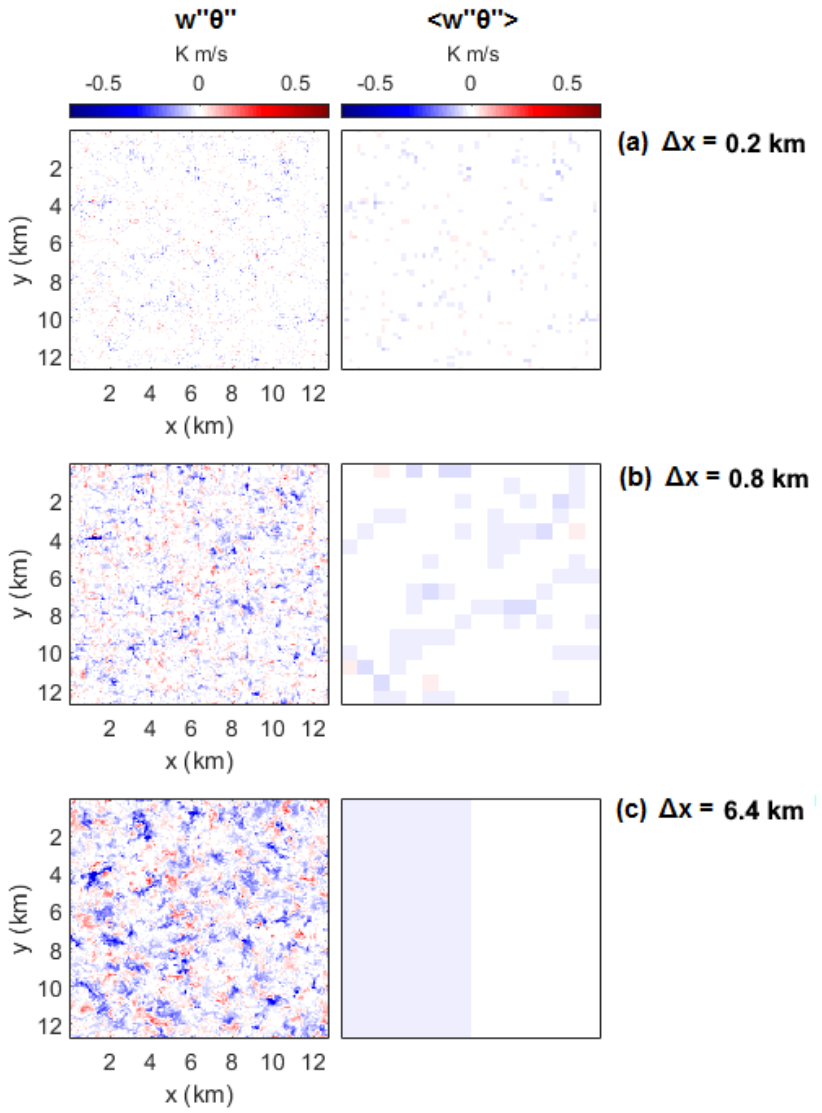

Figure 4: Multiplication of w'' and θ'' yields the field of $w''\theta''$ (left column). Applying the same coarse-graining process that was used for w and θ, gives the subgrid flux field $\langle w''\theta'' \rangle$ (right column). The coarse-grained fields in the second column represent the subgrid fluxes in an NWP model. The mesh size is $\Delta x_{NWP} = 0.2$ km for (a), $\Delta x_{NWP} = 0.8$ km for (b) and $\Delta x_{NWP} = 6.4$ km for (c).

The terms of the form of $\langle u_i'' \phi'' \rangle$ and $\frac{\partial \langle u_i'' \phi'' \rangle}{\partial x_i}$ can be studied by plotting pixel plots (as in Fig. 4) or quantified by plotting their probability density functions. The vertical heat and moisture fluxes are diagnosed first, and are subsequently compared to the results of Honnert et al. (2011). Then we will move on to the horizontal heat and moisture fluxes. In part, we will be able to compare the results for the horizontal fluxes to a previous study by Kurowski and Teixeira (2018). Flux partitioning, as also presented by De Roode et al. (2019), Honnert et al. (2011) and Kurowski and Teixeira (2018), can provide insight into the transition from the entirely subgrid turbulent fluxes at larger grid sizes, to the mostly resolved fluxes at small grid sizes. In addition, it is possible to diagnose K_ϕ with $\langle u_i'' \phi'' \rangle$ and $\frac{\partial \phi}{\partial x_i}$ from the coarse-grained grids. In the rest of this section, it will be described how the coarse-graining process was conducted, how the down-gradient diffusion approach was studied as a method of parametrisation, and finally which LES simulation cases were used.

3.2 Interpolation of LES fields to full and half levels

In an LES staggered grid, velocities u, v and w and scalars ϕ sit at different locations. The scalar quantities are located at the centre of a grid box and the velocity components are located at the face centres.

It can also be said that the scalars sit at the full levels and the velocities sit at the half levels. (see Fig. 5). Since we want to assess fluxes, we will need to determine the values of the velocties at the full levels by linear interpolation. Also, to assess the divergence of fluxes it will be convenient to interpolate the scalar fields to half levels. The interpolations are also important for consistency in the coarse-graining process. When the velocity data points are shifted with a single interpolation to the centre of a grid box, they are given at the same location where temperature, humidity and other scalars are given. This makes it possible to manipulate all data points in the same way.

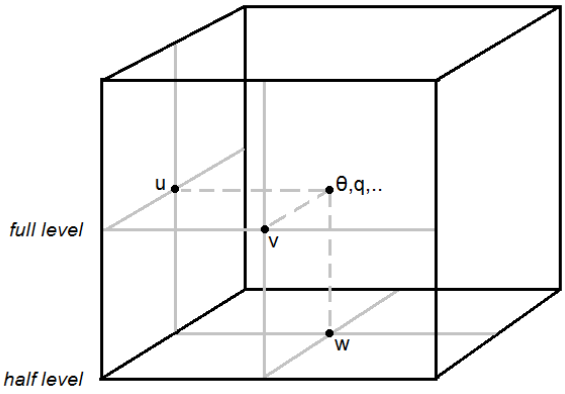

Figure 5: A grid box in a staggered grid structure.

The interpolation method can be applied in the x-, y- or z-direction and as such to velocities u, v and w. In the following, the method is explained for the velocity in the x-direction. Firstly, the grid of the horizontal velocity u is shifted to match the positions of temperature, humidity and other scalars (see Fig. 6(ab)). The data points are shifted by interpolation as in Eq. (16),

$$u_{i,j} = \frac{u_{i-\frac{1}{2},j} + u_{i+\frac{1}{2},j}}{2}. \tag{16}$$

Eq. (16) yields $u_{i,j}$ at the full levels from velocities $u_{i-\frac{1}{2},j}$ and $u_{i+\frac{1}{2},j}$ at two adjacent half levels. The same procedure can be applied to velocities v and w. To calculate the flux divergences, a version of the LES grid is needed where all quantities sit at the half levels (see also Fig. 7(ab)). To this end, the scalars should be interpolated to the half levels as,

$$\phi_{i-\frac{1}{2},j} = \frac{\phi_{i-1,j} + \phi_{i,j}}{2}. \tag{17}$$

This interpolation can also be applied in the y and z-direction. In the remainder of the text we will assume that all velocities and scalars are known at both full and half levels.

The new data set that is created with Eq. (16), in which all velocity and scalar values are located at the grid box centres, will be used to diagnose the coarse-grained mean values. An alternative interpolation method, which uses multiple interpolations to generate a self-similar coarse-grained grid, is described in the appendix. It was ultimately not used in the analysis, because it proved to be more difficult to implement than the method used here.

3.3 Definition of the coarse-graining process

Coarse-graining changes an $N_x \times N_y$ grid into an $M_x \times M_y$ grid with larger grid boxes. Each grid box in the $M_x \times M_y$ grid consists of $n_x \times n_y$ original grid boxes. Coarse-graining to the n^{th} order means that $n_x = n_y = 2^n$ (see Fig. 1). The width of the original grid boxes is called Δx_{LES}, because the original field comes directly from the LES simulation. After coarse-graining the new grid box has a width $\Delta x_{NWP} = 2^n \Delta x_{LES}$, mimicking the grid size that might be used in a numerical weather prediction model. The fluxes $\langle u_i'' \phi'' \rangle$ are found for the coarse-grained field at each grid box size.

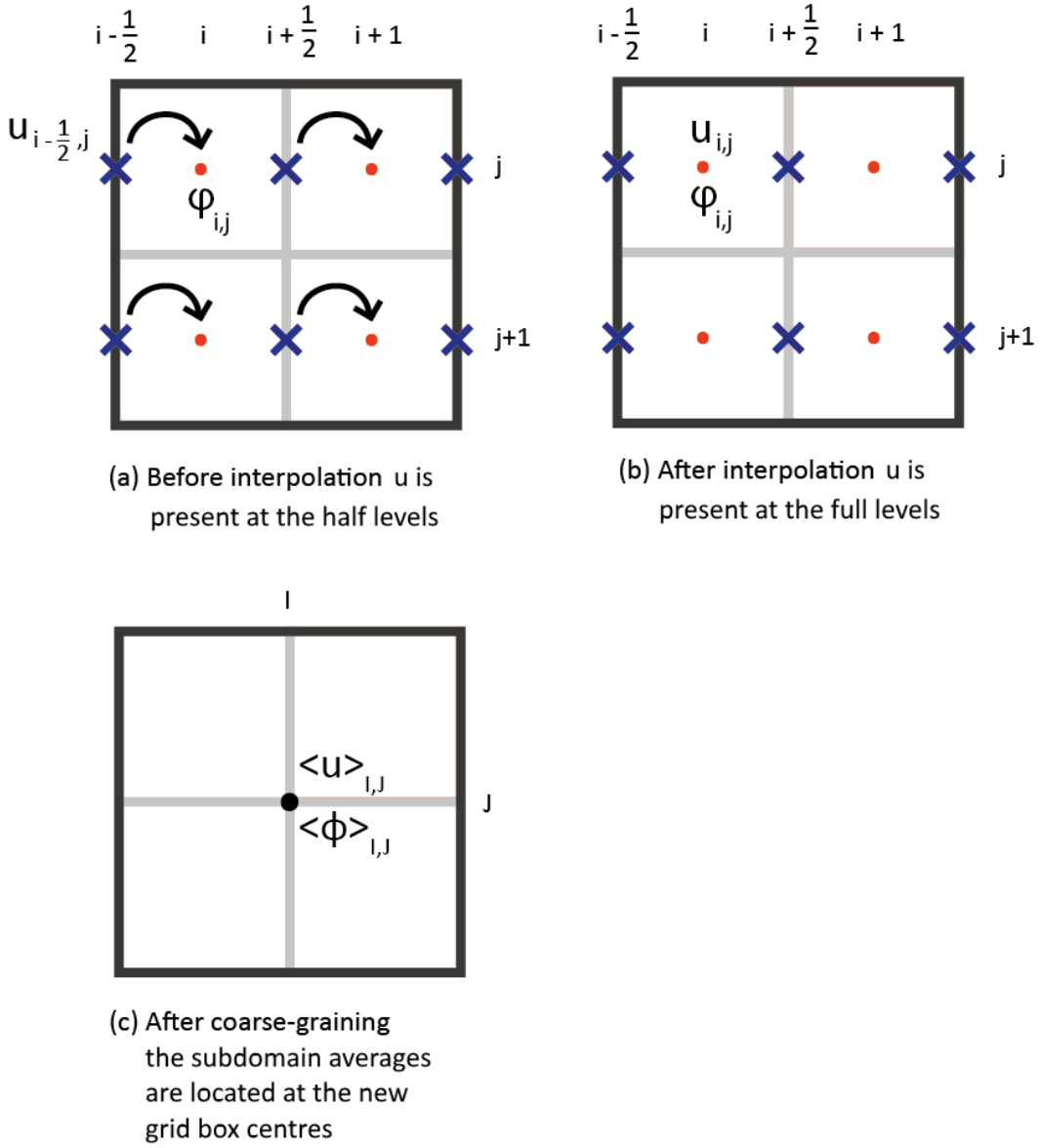

Figure 6: Top-down view of an LES grid box (a) before and (b) after shifting the u-velocity to the full levels. The subdomain averages $\langle\phi\rangle$ and $\langle u\rangle$ are shown in (c), at the centre of the grid boxes.

In the coarse-graining approach the grid the data points are averaged. When $n_x \times n_y$ grid points are averaged, $\langle\phi\rangle$ for the larger grid box is given by,

$$\langle\phi\rangle(z) = \frac{1}{n_x n_y} \sum_{i=1}^{n_x} \sum_{j=1}^{n_y} \phi_{i,j}(z). \tag{18}$$

The subdomain average $\langle\phi\rangle$ is located at the grid box centre of the coarse-grained grid box and has indices I and J in the new $M_x \times M_y$ grid (see Fig. 6(c)). With Eq. (18) scalar averages $\langle\theta\rangle$ and $\langle q_t\rangle$ are determined, as well as the velocities $\langle u\rangle$, $\langle v\rangle$ and $\langle w\rangle$. For every original grid box, velocity fluctuations u'', v'' and w'' and scalar quantity fluctuations ϕ'' can be found with Eq. (19). Velocity fluctuations v'' and w'' are calculated with the equation for u'',

$$\begin{aligned} u''_{i,j} &= u_{i,j} - \langle u\rangle_{I,J} \\ \phi''_{i,j} &= \phi_{i,j} - \langle\phi\rangle_{I,J} \end{aligned}. \tag{19}$$

The fields at the full levels are used to compute the subgid fluxes. The subgrid fluxes $\langle u''\phi''\rangle$ are covariances as described in De Roode et al. (2019). According to De Roode et al. (2019), the subgrid flux $\langle u''\phi''\rangle$ is defined as

$$\langle u''\phi''\rangle_{I,J} = \frac{1}{n_x n_y}\sum_{i=1}^{n_x}\sum_{j=1}^{n_y}(u_{i,j} - \langle u\rangle_{I,J})(\phi_{i,j} - \langle\phi\rangle_{I,J}). \tag{20}$$

The subgrid flux $\langle u''\phi''\rangle$ is located at the centre of the coarse-grained grid box, just like $\langle u\rangle$ and $\langle\phi\rangle$. With this method, information from all original data points is used.

3.4 Consequences of coarse-graining budget equations

To obtain the net effect of the subgrid fluxes on the tendencies of the mean, we need to know the flux divergence. The flux divergence may be determined from the advection term in the scalar equation. We can write the coarse-grained advection term as,

$$\Big\langle \frac{\partial u\phi}{\partial x}\Big\rangle = \frac{\partial\langle u\rangle\langle\phi\rangle}{\partial x} + \Big\langle\frac{\partial u''\phi''}{\partial x}\Big\rangle_{adv} + B. \tag{21}$$

With this advection term it can be derived that the coarse-grained budget equation is given by,

$$\frac{\partial\langle\phi\rangle}{\partial t} = -\langle u_i\rangle\frac{\partial\langle\phi\rangle}{\partial x_i} - \Big\langle\frac{\partial u_i''\phi''}{\partial x_i}\Big\rangle - B. \tag{22}$$

Interestingly, the averaging operator $\langle.\rangle$ is outside the differential operator in Eqs. (21) and (22), which is not how the subgrid transport term is written in the NWP budget equation in Eq. (14). Also, some contributions B appear in Eq. (22), that are not present in Eq. (14). The full derivation of Eqs. (21) and (22) and the additional term B is given in appendix B.

The subgrid transport term plus additional terms $\langle\frac{\partial u''\phi''}{\partial x}\rangle_{adv} + B$ for every subdomain can be diagnosed from the difference between $\langle\frac{\partial u\phi}{\partial x}\rangle$ and $\frac{\partial\langle u\rangle\langle\phi\rangle}{\partial x}$. The quantities needed can be found from the coarse-grained LES fields. Numerically, $\langle\frac{\partial u\phi}{\partial x}\rangle$ can be determined as follows,

$$\Big\langle\frac{\partial u\phi}{\partial x}\Big\rangle_{I,J} = \frac{1}{n_x n_y}\sum_{i=1}^{n_x}\sum_{j=1}^{n_y}\frac{u_{i+\frac{1}{2},j}\phi_{i+\frac{1}{2},j} - u_{i-\frac{1}{2},j}\phi_{i-\frac{1}{2},j}}{\Delta x_{LES}}, \tag{23}$$

and $\frac{\partial\langle u\rangle\langle\phi\rangle}{\partial x}_{I,J}$ can be found by using the differentation product rule,

$$\begin{aligned}\frac{\partial\langle u\rangle\langle\phi\rangle}{\partial x}_{I,J} &= \langle u\rangle\frac{\partial\langle\phi\rangle}{\partial x} + \langle\phi\rangle\frac{\partial\langle u\rangle}{\partial x}\\ &= \langle u\rangle_{I,J}\frac{\langle\phi\rangle_{I+1,J} - \langle\phi\rangle_{I-1,J}}{2\Delta x_{NWP}} + \langle\phi\rangle_{I,J}\frac{\langle u\rangle_{I+1,J} - \langle u\rangle_{I-1,J}}{2\Delta x_{NWP}}.\end{aligned} \tag{24}$$

If B is small, the difference between $\langle\frac{\partial u\phi}{\partial x}\rangle$ and $\frac{\partial\langle u\rangle\langle\phi\rangle}{\partial x}$ gives the flux divergence. To estimate the magnitude of the boundary terms and see if they are indeed small, we can quantify the flux divergence $\langle\frac{\partial u''\phi''}{\partial x}\rangle$ directly from the LES field and compare it to $\langle\frac{\partial u''\phi''}{\partial x}\rangle_{adv} + B$.

3.5 Direct diagnosis of the flux divergence from LES fields

The flux divergences that are found directly from the LES field are indicated as $\langle \frac{\partial u''\phi''}{\partial x} \rangle_{dir}$. In order to find the flux divergence from the LES field, first the flux gradient $(\frac{\partial u''\phi''}{\partial x})_{i,j}$ is obtained at every grid point and then $(\frac{\partial u''\phi''}{\partial x})_{i,j}$ is averaged over a subdomain. In order to find the flux gradients at every grid box, it is convenient to use the velocity and scalar values at the half levels (see also Fig. 5). On every grid box border $u''\phi''_{i-\frac{1}{2},j} = (u_{i-\frac{1}{2},j} - \langle u \rangle_{I,J})(\phi_{i-\frac{1}{2},j} - \langle \phi \rangle_{I,J})$ is known from the velocities and interpolated scalar values. Then, to obtain $(\frac{\partial u''\phi''}{\partial x})_{i,j}$ at the grid box centre i, the difference between $u''\phi''$ for $i + \frac{1}{2}$ and for $i - \frac{1}{2}$ is used. As is illustrated in Fig. 7, $(\frac{\partial u''\phi''}{\partial x})_{i,j}$ is then given by,

$$\left(\frac{\partial u''\phi''}{\partial x} \right)_{i,j} = \frac{u''\phi''_{i+\frac{1}{2},j} - u''\phi''_{i-\frac{1}{2},j}}{\Delta x_{LES}}. \tag{25}$$

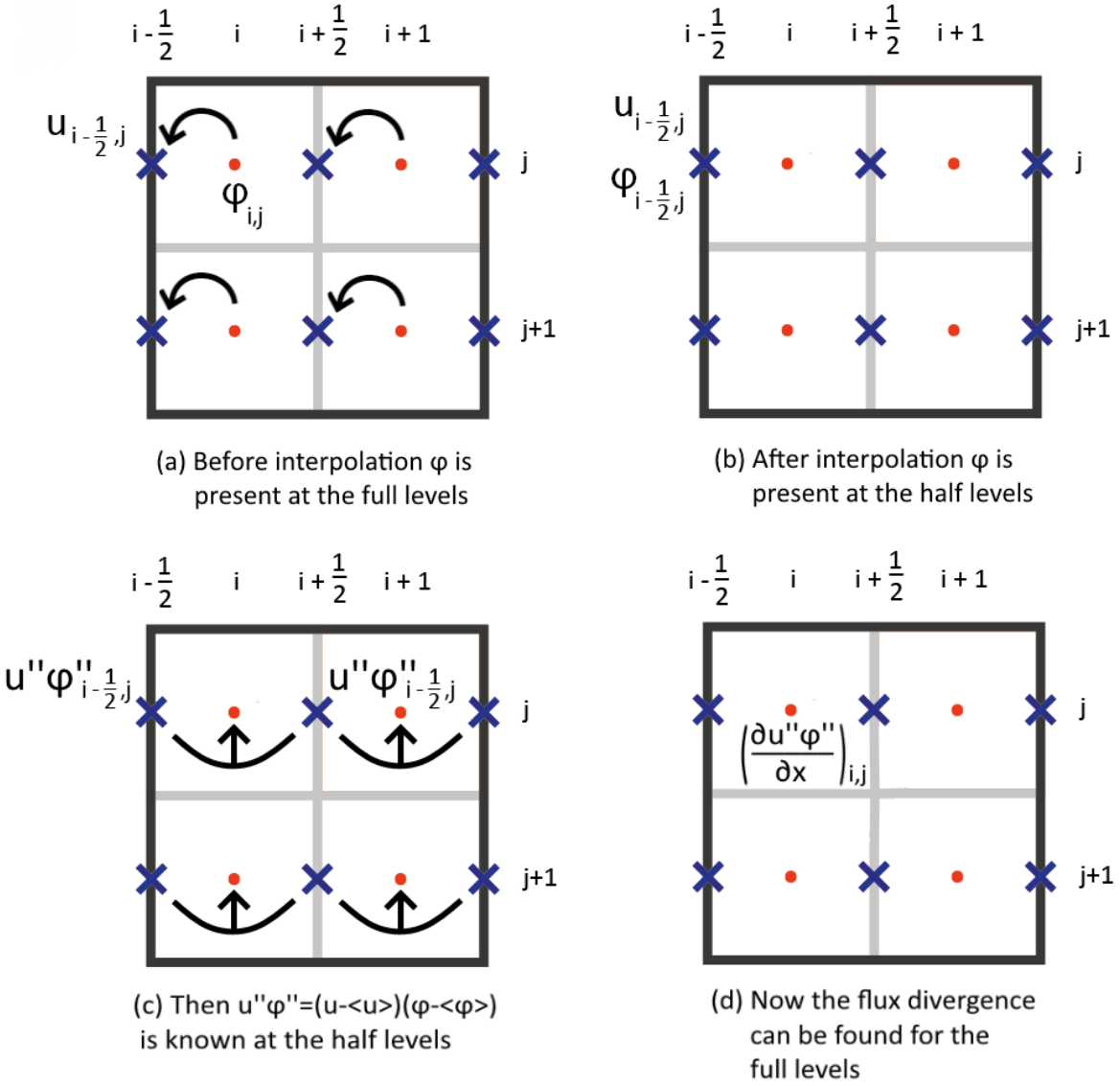

Figure 7: The process used to obtain $\left(\frac{\partial u''\phi''}{\partial x} \right)_{i,j}$ at every grid point.

The subgrid flux divergence $\langle \frac{\partial u''\phi''}{\partial x} \rangle_{dir}$ can be determined from Eq. (25) by averaging over a subdomain. The averaging process is given in the following steps. First the averaging operator is used on $(\frac{\partial u''\phi''}{\partial x})_{i,j}$ (Eq. (18)),

$$\left\langle \frac{\partial u''\phi''}{\partial x} \right\rangle_{dir\ I,J} = \frac{1}{n_x n_y} \sum_{i=1}^{n_x} \sum_{j=1}^{n_y} \left(\frac{\partial u''\phi''}{\partial x} \right)_{i,j}. \tag{26}$$

Then it follows from Eq. (25) that,

$$\left\langle \frac{\partial u''\phi''}{\partial x} \right\rangle_{dir\ I,J} = \frac{1}{n_x n_y} \sum_{i=1}^{n_x} \sum_{j=1}^{n_y} \frac{u''\phi''_{i+\frac{1}{2},j} - u''\phi''_{i-\frac{1}{2},j}}{\Delta x_{LES}}. \tag{27}$$

Because the inner flux terms cancel each other, the only terms left after the summation in the x-direction are the fluxes on the subdomain borders (at indices $\frac{1}{2}$ and $n_x + \frac{1}{2}$). This is illustrated in Fig. 8. Also, it holds that $n_x \Delta x_{LES} = \Delta x_{NWP}$. So the final result for $\langle \frac{\partial u''\phi''}{\partial x} \rangle_{dir\ I,J}$ is

$$\left\langle \frac{\partial u''\phi''}{\partial x} \right\rangle_{dir\ I,J} = \frac{1}{n_y} \sum_{j=1}^{n_y} \frac{u''\phi''_{n_x+\frac{1}{2},j} - u''\phi''_{\frac{1}{2},j}}{\Delta x_{NWP}}. \tag{28}$$

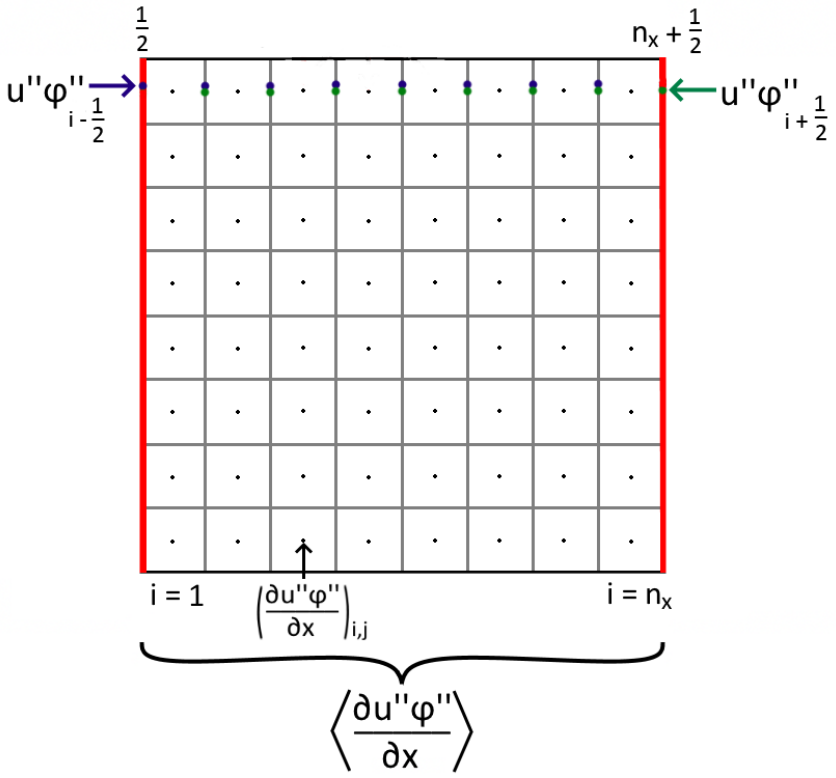

Figure 8: Determination of the flux divergence for one coarse-grained grid box. Because the $u''\phi''$ terms cancel each other, only the borders of the subdomain contribute to the flux divergence $\langle \frac{\partial u''\phi''}{\partial x} \rangle_{dir\ I,J}$.

For $\langle \frac{\partial u''\phi''}{\partial x} \rangle_{dir\ I,J}$, the only $u''\phi''$ terms that contribute are located at the borders. The internal dynamics are not important when diagnosing $\langle \frac{\partial u''\phi''}{\partial x} \rangle_{dir\ I,J}$, since the interior fluxes do not impact the mean value of the subdomain. Therefore it is possible to calculate $\langle \frac{\partial u''\phi''}{\partial x} \rangle_{dir\ I,J}$ with just the values of $u''_{i-\frac{1}{2},j}$ and $\phi''_{i-\frac{1}{2},j}$ at the borders.

From the flux divergence $\langle \frac{\partial u''\phi''}{\partial x} \rangle$ we can find the net effect of the subgrid fluxes on the tendencies of the mean of scalars like θ, θ_v and q_t. However, $\langle \frac{\partial u''\phi''}{\partial x} \rangle$ is not the form that is present in the governing

equation of NWP models that expresses this tendency of the mean (see Eq. (14)). Instead the form $\frac{\partial\langle u''\phi''\rangle}{\partial x}$ is used. If we determine $\frac{\partial\langle u''\phi''\rangle}{\partial x}$ from $\langle\frac{\partial u''\phi''}{\partial x}\rangle$, we take the averaging operator inside of the differential operator. Then another term $B_{u''\phi''}$ appears (see appendix B),

$$\left\langle \frac{\partial u''\phi''}{\partial x} \right\rangle = \frac{\partial\langle u''\phi''\rangle}{\partial x} + B_{u''\phi''}. \tag{29}$$

According to Eq. (29), writing $\frac{\partial\langle u''\phi''\rangle}{\partial x}$ in the NWP budget equation is only justified if $B_{u''\phi''}$ is small. To estimate the magnitude of $B_{u''\phi''}$, we find $\frac{\partial\langle u''\phi''\rangle}{\partial x}$ from the LES fields. Using the subgrid fluxes obtained according to Eq. (20), we obtain the flux divergence $\frac{\partial\langle u''\phi''\rangle}{\partial x}_{I,J}$ as,

$$\frac{\partial\langle u''\phi''\rangle}{\partial x}_{I,J} = \frac{\langle u''\phi''\rangle_{I+1,J} - \langle u''\phi''\rangle_{I-1,J}}{2\Delta x_{NWP}}. \tag{30}$$

Note that for $\frac{\partial\langle u''\phi''\rangle}{\partial x}_{I,J}$ the subgrid fluxes are averaged over a subdomain before a gradient is taken.

In chapter 4.2, a comparison is given of $\langle\frac{\partial u''\phi''}{\partial x}\rangle_{adv}$, $\langle\frac{\partial u''\phi''}{\partial x}\rangle_{dir}$ and $\frac{\partial\langle u''\phi''\rangle}{\partial x}$, in order to diagnose the importance of B and $B_{u''\phi''}$.

3.6 Down-gradient diffusion model

In current NWP models a parametrisation is already utilised to calculate the subgrid fluxes (see Boutle et al. (2014)). The fluxes are given by a down-gradient diffusion approach based on K-theory and can be given as follows,

$$\langle u_i''\phi''\rangle = -K_{h,i}\frac{\partial\langle\phi\rangle}{\partial x_i}. \tag{31}$$

Here $\langle u_i''\phi''\rangle$ is the subgrid flux, $K_{h,i}$ is eddy diffusivity in direction i, and ϕ is the average scalar over the grid box. Note that this parametrisation scheme is similar to that used in LES (see Eq. (8)). The eddy diffusivity K can be found with the following closure hypothesis,

$$K = c\sqrt{e}l. \tag{32}$$

The constant c is an undetermined constant, $e = \frac{1}{2}(\langle u''^2\rangle + \langle v''^2\rangle + \langle w''^2\rangle)$ is the subgrid turbulent kinetic energy and l is the mixing length. For a CBL, l is typically taken to represent the dominant eddy size. Following Deardorff (1980), the length scale is taken equal to the size of the grid for which the subgrid fluxes are calculated. In this case we diagnose the subgrid fluxes and eddy diffusivity in the NWP model, so $l = \Delta x_{NWP}$.

The coarse-graining process generates a grid of all quantities at the full levels. The left-hand side of Eq. (31) can be calculated with Eq. (20). The right-hand side can be obtained if the average temperature gradient is known. The average vertical temperature gradient $\frac{\partial\langle\phi\rangle}{\partial z}$ and the average horizontal temperature gradient $\frac{\partial\langle\phi\rangle}{\partial x}$ can be found with Eq. (33), using the average temperature $\langle\phi\rangle$ from Eq. (18),

$$\begin{aligned}\frac{\partial\langle\phi\rangle}{\partial z}_{I,J,k} &= \frac{\langle\phi\rangle_{I,J,k+1} - \langle\phi\rangle_{I,J,k-1}}{2\Delta z}\\ \frac{\partial\langle\phi\rangle}{\partial x}_{I,J,k} &= \frac{\langle\phi\rangle_{I+1,J,k} - \langle\phi\rangle_{I-1,J,k}}{2\Delta x_{NWP}}.\end{aligned} \tag{33}$$

To get a more specific idea of the eddy diffusivity K_h, we look at the case of the vertical and horizontal moisture flux $\langle w''q_t''\rangle$ and $\langle u''q_t''\rangle$. The vertical moisture flux has a strictly positive vertical profile below the inversion, which will make it easier to interpret. We define $\langle K_{q_t,z}\rangle$ and $\langle K_{q_t,x}\rangle$ for each subdomain as,

$$\langle K_{q_t,z} \rangle = -\frac{\langle w'' q_t'' \rangle}{\partial \langle q_t \rangle / \partial z}$$
$$\langle K_{q_t,x} \rangle = -\frac{\langle u'' q_t'' \rangle}{\partial \langle q_t \rangle / \partial x}. \tag{34}$$

We are interested in the dependency of $K_{q_t,z}$ and $K_{q_t,x}$ on z/z_i and $\Delta x_{NWP}/z_i$. Note that current parametrisations assume isotropy for K. We will assess whether an isotropic assumption is still valid at NWP grid sizes. In chapter 4.3, the analysis method for the K-diffusion is elaborated on and the results are shown.

3.7 Simulation cases

Two different simulation cases are analysed to probe the influence of the input parameters on the results. We will investigate two different CBL cases, based on the CBL case in De Roode et al. (2004). The first simulation, which we will call *case CBL*, provides a convective boundary layer with large-scale fluctuations. This will allow us to look at well-developed heat and moisture fluxes. In Fig. 9(a) the vertical profiles of the resolved and subgrid fluxes of heat, moisture and buoyancy are shown, determined from LES for case CBL. Because of the large humidity flux at the surface, the buoyancy flux $\overline{w'\theta'_v}$ is much different from the heat flux $\overline{w'\theta'}$. The fluxes $\overline{w'\theta'}$, $\overline{w'q'_t}$ and $\overline{w'\theta'_v}$ are interconnected as

$$\overline{w'\theta'_v} = \overline{w'\theta'} + \left(\frac{R_v}{R_d} - 1\right) \bar{\theta}\, \overline{w'q'_t}. \tag{35}$$

Here, R_v and R_d are the specific gas constants for water vapour and dry air, respectively. The value for $\frac{R_v}{R_d} - 1$ is often approximated to 0.61. It will be interesting to study $\overline{w'\theta'_v}$, because the fluctuations in θ_v are smaller than those in θ and q_t. This was previously shown in De Roode et al. (2004). Furthermore, $\overline{w'\theta'_v}$ will show how the heat fluxes would behave in a dry CBL, since in a dry CBL it holds that $\overline{w'q'_t} = 0$ and so $\overline{w'\theta'} = \overline{w'\theta'_v}$. As such, we do not need to simulate a dry CBL separately.

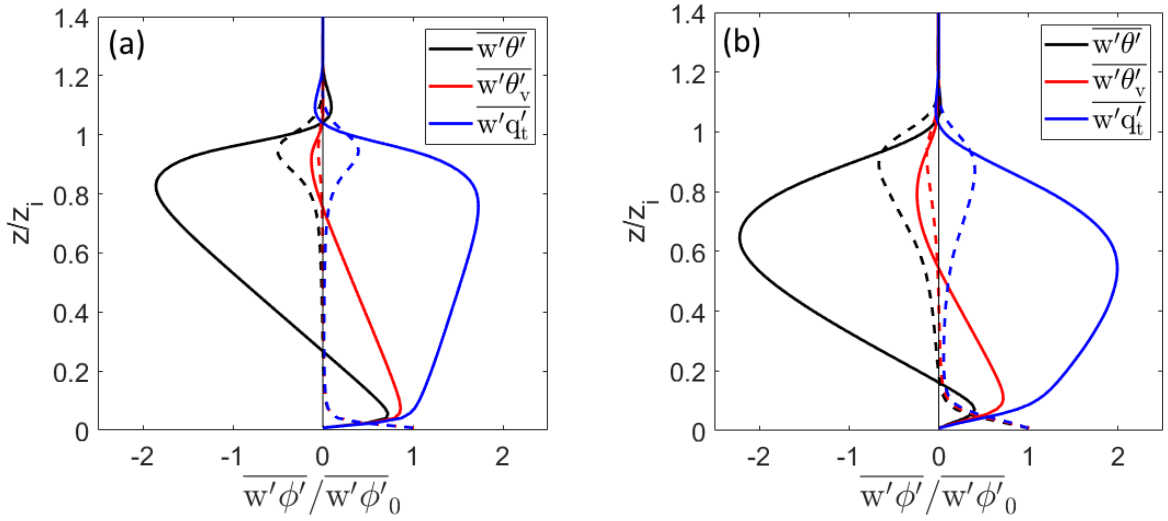

Figure 9: Slab-average vertical flux profiles of the LES resolved (solid lines) and subgrid (dashed lines) contributions to the heat flux, buoyancy flux and moisture flux, averaged over the last 60 s of hour 8. In (a), flux profiles are given for case CBL and in (b) they are given for CBL_{ws}. The height is normalised by the boundary layer height z_i and the fluxes are normalised by the surface values, which have been given a subscript 0.

The second simulation, *case* CBL_{ws}, investigates the impact of wind shear. Case CBL does not have a strongly developed momentum flux $\overline{u'w'}$, because the wind speeds are relatively low. In order to increase

the momentum flux, we need to apply a strong wind shear in the boundary layer. Therefore, in case CBL_{ws} the wind speed in the boundary layer and the geostrophic wind in the x-direction are increased from 1.0 m/s to 15.0 m/s. It is also necessary to introduce subsidence, so that the boundary does not grow into the sponge layer during the simulation. The divergence D, which is a measure for the horizontal air displacement due to subsidence, is set to $3 \times 10^{-5}\ s^{-1}$. In Fig. 9(b), the height profiles of the vertical heat, moisture and buoyancy flux are given for case CBL_{ws}. Compared to case CBL, the inversion is located at about the same height for case CBL_{ws}.

The input parameters for case CBL and case CBL_{ws} are given in Tab. 1 and include the surface pressure, the wind speeds, the surface fluxes, the divergence, the runtime of the simulation and the statistical intervals. The input height profiles for potential temperature and humidity, shown in Fig. 10, are the same for both simulations. The domain size of the simulations is $12.8 \times 12.8 \times 2.56$ km, with $\Delta x_{LES} =$ 50 m and $\Delta z = 20$ m. The horizontal domain size is denoted by L_x.

Table 1: Input parameters of simulation cases CBL and CBL_{ws}. Surface pressure p_s, the geostrophic winds U_{geo} and V_{geo}, horizontal wind speeds U and V, surface fluxes for heat and moisture $\langle w'\theta' \rangle_0$ and $\langle w'q'_{\text{t}} \rangle_0$, and divergence D are indicated below. The simulation runs for 10 hours in every case and returns statistics every minute.

Quantity	Units	Case CBL	Case CBL_{ws}
p_s	hPa	1040	1040
U_{geo}	m/s	1.0	15.0
V_{geo}	m/s	0.0	0.0
U	m/s	1.0	15.0
V	m/s	0.0	0.0
$\langle w'\theta'_l \rangle_0$	K m/s	0.025	0.025
$\langle w'q'_t \rangle_0$	kg/kg m/s	1.366×10^{-4}	1.366×10^{-4}
Div	s^{-1}	0.0	3×10^{-5}
runtime	h	10	10
statistical intervals	s	60	60

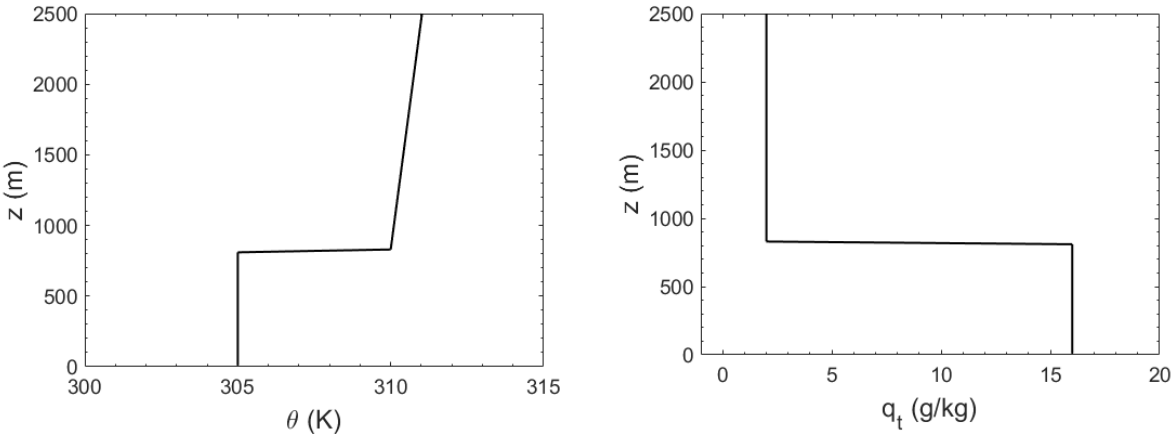

Figure 10: Initial vertical profiles for θ and q_{t} for both simulation cases.

Fig. 9 also gives the LES subgrid fluxes for heat, moisture and buoyancy for both simulation cases. The LES subgrid fluxes in case CBL are clearly very small everywhere in the boundary layer, except at the surface and in the entrainment zone. For case CBL_{ws}, very small values of the subgrid flux are only found between heights $z/z_i = 0.1$ and $z/z_i = 0.4$. To understand how the LES resolved and subgrid fluxes relate to the NWP subgrid fluxes we want to study, we look at how resolved, subgrid and total turbulent fluxes are connected in LES and NWP models.

In general, the total slab-averaged flux $\overline{u_i'\phi'}$ of a quantity is given by the sum of its resolved and subgrid parts at a particular grid size, which are denoted by $\overline{u_i'\phi'}_{res}$ and $\overline{u_i'\phi'}_{sub}$ respectively (see also Honnert et al. (2011)). So for the resolved and subgrid fluxes at the LES and NWP grid sizes we can write,

$$\overline{u_i'\phi'} = \overline{u_i'\phi'}_{res}^{LES} + \overline{u_i'\phi'}_{sub}^{LES} = \overline{u_i'\phi'}_{res}^{NWP} + \overline{u_i'\phi'}_{sub}^{NWP}. \tag{36}$$

The superscript LES indicates that the fluxes are determined for grid size Δx_{LES} and NWP indicates that they are determined for grid size Δx_{NWP}. In this study, we are interested in the subgrid fluxes of NWP models. The resolved and subgrid fluxes at the NWP grid size are determined from the resolved velocities and scalars in the LES fields. In the LES grid the total flux is made up of the LES resolved flux and the subfilter-scale flux. We do not include the LES subfilter flux, so the LES resolved flux represents the total slab-averaged flux. Then the resolved and subgrid fluxes for the NWP model sum to the LES resolved flux and as such to the total slab-averaged flux. Excluding LES sub-filter fluxes is reasonable, because they are small everywhere in the boundary layer, except at the surface and the entrainment zone. This is visible in Fig. 9 and was also shown previously by Nieuwstadt et al. (1993). However, for case $\mathrm{CBL_{ws}}$, the LES subgrid fluxes are significant in most of the boundary layer. This should be taken into account when interpreting the results for NWP resolved and subgrid fluxes in case $\mathrm{CBL_{ws}}$.

4 Results and Discussion

4.1 Vertical flux behaviour

Vertical fluxes are studied to assess the validity of the analysis method used. If the results for the vertical fluxes agree with the literature, we can confidently apply the same methodology to the horizontal fluxes to obtain new results. For the vertical fluxes, only the results for case CBL are shown, because the results for case CBL and case $\mathrm{CBL_{ws}}$ are very similar for the heat fluxes, moisture fluxes and buoyancy fluxes that were studied. Firstly, pixel plots of the subgrid and resolved fluxes visualise the transition from entirely resolved to entirely subgrid fluxes in the grey zone. In Fig. 11 the vertical resolved and subgrid heat fluxes are given at $z/z_i = 0.5$. Similar results were obtained for the moisture fluxes (not shown). At small Δx_{NWP} turbulence is largely resolved, so the resolved flux shows detailed structures as well. These disappear at about $\Delta x_{NWP} = 1.6$ km, which is about as large as the boundary layer height ($z_i =$ 1200 m at $t = 8$ h). At this grid size, even the largest eddies at the scale of the boundary layer cannot be resolved any more. The subgrid flux is small at first and then starts to take over some of the structures from the resolved flux. For very large Δx_{NWP}, the subgrid flux converges to -0.02 $\mathrm{Kms^{-1}}$.

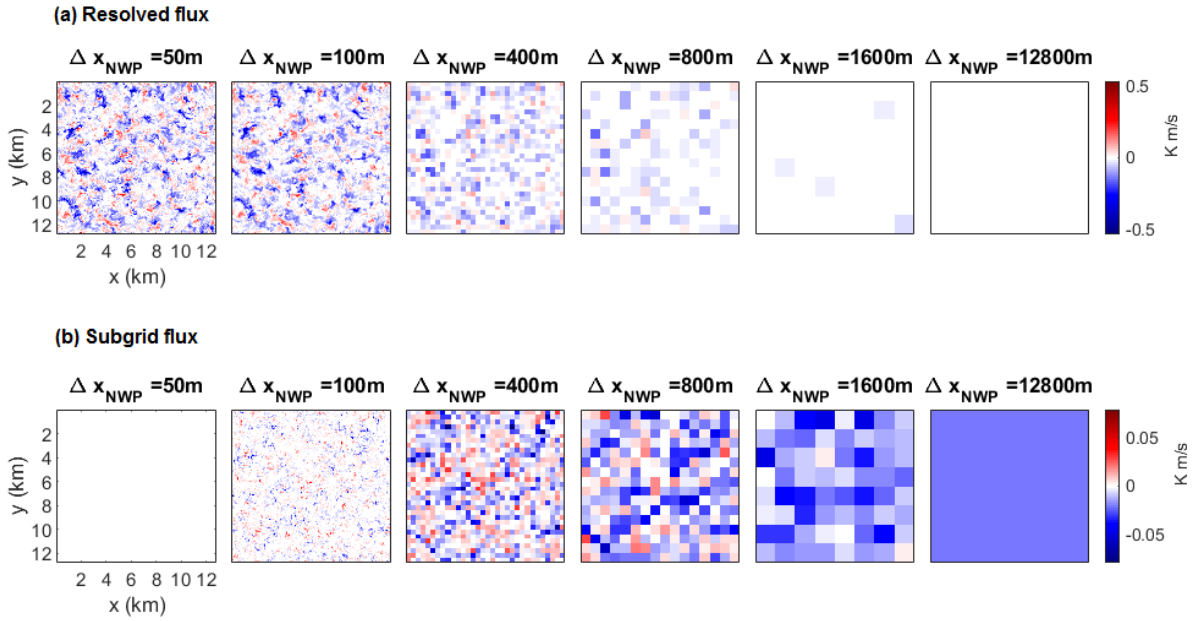

Figure 11: (a) Pixel plots of the vertical resolved heat flux $w''\theta''_{res} = (\langle w \rangle - \overline{w})(\langle \theta \rangle - \overline{\theta})$ and (b) pixel plots of the vertical subgrid heat flux $\langle w''\theta'' \rangle$, using instantaneous values at $t = 8$ h, for $z/z_i = 0.5$ and case CBL.

The transition from resolved to subgrid turbulent fluxes can also be visualised with flux partitioning, as shown by for example Honnert et al. (2011), Shin and Hong (2013) and Kurowski and Teixeira (2018). Partition plots visualise the subgrid and resolved parts of the turbulent fluxes. The subgrid and resolved parts averaged over the entire LES domain are defined as in De Roode et al. (2019),

$$\overline{\phi'\psi'}_{res} = \frac{1}{M_x M_y} \sum_{k=1}^{M_x} \sum_{l=1}^{M_y} (\langle \phi \rangle_{kl} - \overline{\phi})(\langle \psi \rangle_{kl} - \overline{\psi}) \tag{37}$$

$$\overline{\phi'\psi'}_{sub} = \frac{1}{M_x M_y} \sum_{k=1}^{M_x} \sum_{l=1}^{M_y} \langle \phi''\psi'' \rangle_{kl}. \tag{38}$$

In Fig. 12, the slab-averaged and normalised values of the resolved and subgrid heat flux divided by the total flux, $\overline{w'\theta'}_{res}/\overline{w'\theta'}$ and $\overline{w'\theta'}_{sub}/\overline{w'\theta'}$, are plotted against $\Delta x_{NWP}/z_i$. Note that the total flux $\overline{w'\theta'}$ is equal to the LES resolved flux, because the LES subgrid fluxes are neglected (see also chapter 3.7). Fig. 12 shows that at small Δx_{NWP} the turbulence is entirely resolved, and $\overline{w'\theta'}_{res}/\overline{w'\theta'} = 1$. This is reflected

in the pixel plot of the resolved flux at $\Delta x_{NWP} = 50$ m in Fig. 11, where the resolved flux has detailed structures. After $\Delta x_{NWP}/z_i = 0.8$ the subgrid contribution to the turbulent flux becomes larger than the resolved. In this intermediate range between the LES and NWP limit, the pixel plots show how the structures in the resolved and subgrid fluxes change.

Finally, the turbulence is entirely subgrid as $\overline{w'\theta'}_{sub}/\overline{w'\theta'} = 1$ and $\overline{w'\theta'}_{res}/\overline{w'\theta'} = 0$, when Δx_{NWP} is equal to the domain size. Indeed, the pixel plots show that the resolved flux becomes 0 for $\Delta x_{NWP}/z_i = 10.6$. In Honnert et al. (2011), Shin and Hong (2013) and Kurowski and Teixeira (2018), we also see that the turbulence is entirely subgrid for $\Delta x_{NWP}/z_i \sim 10$.

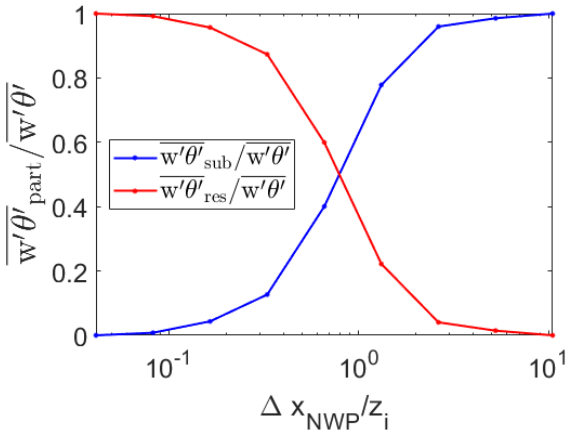

Figure 12: Flux partitioning for the heat flux determined from instantaneous values at $t = 8$ h, for $z/z_i = 0.5$ and case CBL.

The dependency of the variability of the subgrid fluxes on NWP grid size can also be visualised in a probability density function, or PDF (Fig. 13 (a)). The PDFs are plotted for different values of Δx_{NWP}. A PDF is normalised by the total amount of data points, so that the integral over the PDF equals unity. According to Fig. 13(a), the PDF is narrowest for small Δx_{NWP}. This makes sense, because for small Δx_{NWP} the values of the original field and the coarse-grained field do not differ much and thus the fluctuations are small. The distribution becomes broader for larger Δx_{NWP}, as the original LES values differ more from the subdomain mean values in the coarse-grained field and so the fluctuations increase. If the fluctuations increase, so do the subgrid fluxes. As in the pixel plots, it evident in the PDFs that the vertical flux reduces to a single value for $\Delta x_{NWP} = L_x$.

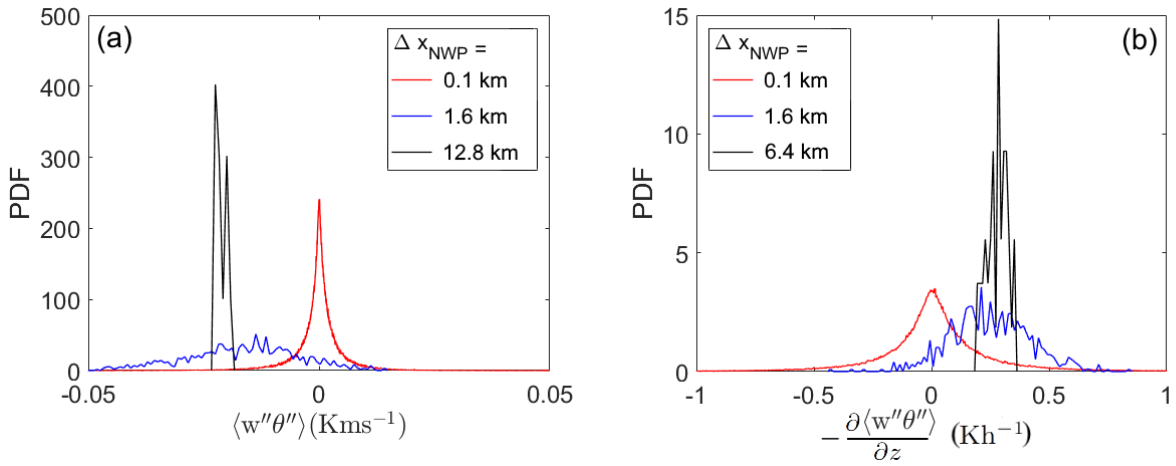

Figure 13: Distribution of (a) the vertical subgrid heat fluxes $\langle w''\theta''\rangle$ and (b) flux divergences $-\frac{\partial\langle w''\theta''\rangle}{\partial z}$ for $z/z_i = 0.5$ and case CBL. The distributions are created from multiple LES fields sampled every 5 minutes between $t = 7$ h and $t = 8$ h. The horizontal axis is limited from -0.05 to 0.05 Kms^{-1} in (a) and from -1 to 1 Kh^{-1} in (b).

In addition, Fig. 13(b) shows how the PDFs for the vertical flux divergence $\frac{\partial\langle w''\phi''\rangle}{\partial z}$ depend on NWP grid size. The distribution for $\frac{\partial\langle w''\phi''\rangle}{\partial z}$ is narrow around zero for small Δx_{NWP} and spreads out for larger values. This makes sense, because the fluctuations from the local subdomain average become larger as

Δx_{NWP} increases. The value of $\frac{\partial \langle w'' \theta'' \rangle}{\partial z}$ at $\Delta x_{NWP} = L_x$ is 0.3 Kh^{-1}. The width of the distribution at $\Delta x_{NWP} = 1.6$ km is about 1 Kh^{-1}, which indicates the order of magnitude with which the vertical subgrid transport influences the tendencies of the mean. Also, note that $\frac{\partial \langle w'' \theta'' \rangle}{\partial z}$ is equal to $\langle \frac{\partial w'' \theta''}{\partial z} \rangle$, while $\frac{\partial \langle u'' \theta'' \rangle}{\partial x}$ and $\langle \frac{\partial u'' \theta''}{\partial x} \rangle$ are not the same (see appendix B for details).

The subgrid fluxes can be slab-averaged to obtain $\overline{w'\theta'}_{sub}$, $\overline{w'\theta'_{\mathrm{v}}}_{sub}$, $\overline{w'q'_{\mathrm{t}}}_{sub}$ and $\overline{w'w'}_{sub}$, following Eq. (38). In Fig. 14 the slab-averaged subgrid fluxes for θ, q_{t} and θ_{v} are plotted against z/z_i. The transition from resolved to subgrid turbulent fluxes is clearly visible, as $\overline{w'\theta'}_{sub}$, $\overline{w'q'_{\mathrm{t}}}_{sub}$ and $\overline{w'\theta'_{\mathrm{v}}}_{sub}$ are zero for $\Delta x_{NWP} = \Delta x_{LES}$ and follow the profile for the total slab-averaged flux for $\Delta x_{NWP} = L_x$ (black line). So, at $\Delta x_{NWP} = L_x$ the subgrid fluxes account for all turbulent transport. The difference between the fluxes for θ, θ_{v} and q_{t} is also apparent. The total vertical fluxes for θ and θ_{v} switch sign at $z/z_i = 0.27$ and $z/z_i = 0.78$, respectively. These critical values of z/z_i will be denoted by $(z/z_i)_c$. The fluxes of θ and θ_{v} switch sign at that particular $(z/z_i)_c$, because the $\frac{\partial \overline{\theta}}{\partial z} < 0$ for $z/z_i < (z/z_i)_c$ and $\frac{\partial \overline{\theta}}{\partial z} > 0$ for $z/z_i > (z/z_i)_c$. In contrast, the total vertical fluxes for q_{t} are strictly positive in the boundary layer, because $\frac{\partial q_{\mathrm{t}}}{\partial z} < 0$ everywhere in the boundary layer. This difference in the total vertical flux profiles continues in the subgrid vertical flux profiles (coloured lines in Fig. 16). The subgrid moisture flux is strictly positive in the boundary layer for every value of Δx_{NWP}. The height profile of the subgrid fluxes of θ and θ_{v} switch sign like the total vertical flux profile does, but the profiles cross zero at larger z/z_i. This can account for some interesting phenomena in the flux partitioning.

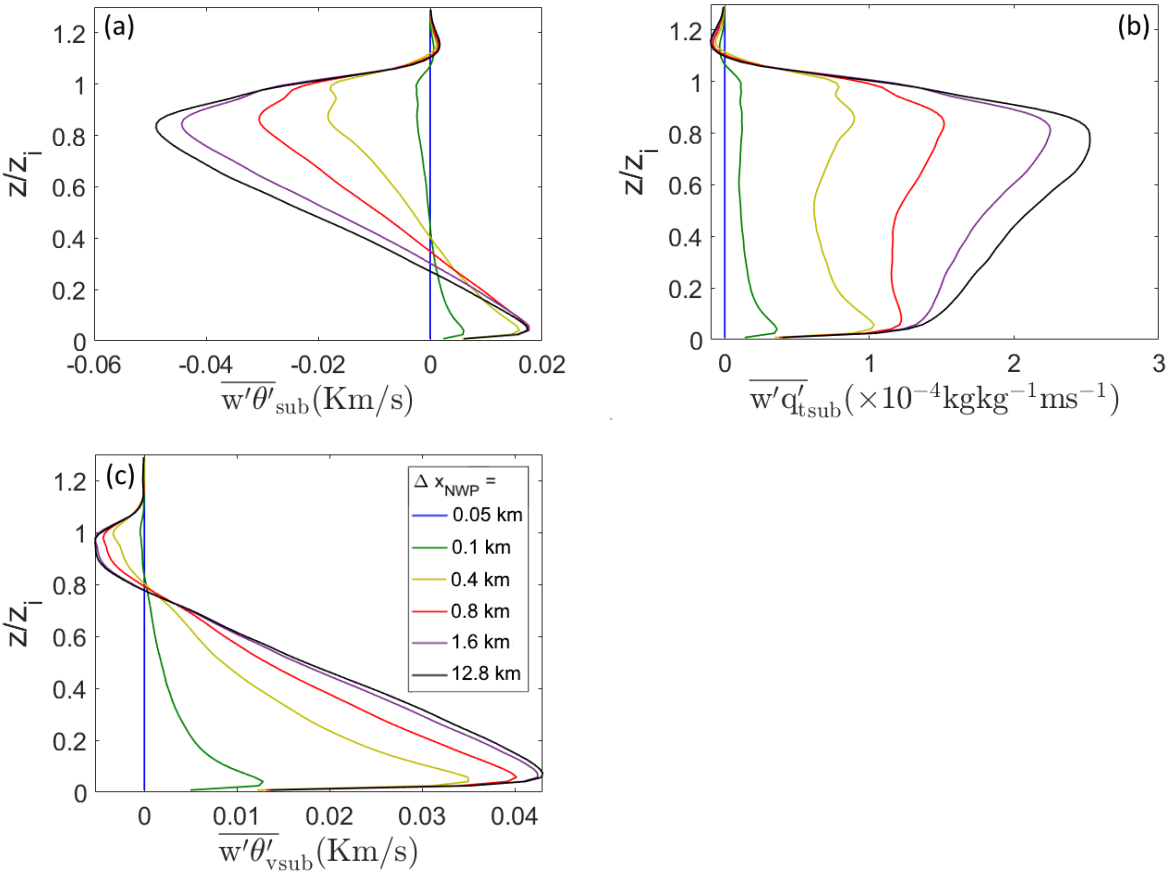

Figure 14: Height profiles for the vertical subgrid (a) heat fluxes, (b) moisture fluxes and (c) buoyancy fluxes for different Δx_{NWP}, determined from instantaneous values at $t = 8$ h in case CBL.

In order to compare the vertical turbulent fluxes $\overline{w'\theta'}$, $\overline{w'\theta'_{\rm v}}$, $\overline{w'q'_{\rm t}}$ and $\overline{w'w'}$, flux partitioning of the subgrid fluxes is shown in Fig. 15 for $z/z_i = 0.1$-0.9. These plots elaborate on the plot in Fig. 12 by comparing the subgrid flux partitioning for heat fluxes, moisture fluxes, buoyancy fluxes and vertical velocity variance in one figure. The x-axis has a logarithmic scale, to better visualise the transition. A number of behaviours are notable. Firstly, the shape of the flux partitioning is different for $z/z_i = 0.1$-0.2 than at any other height. At small Δx_{NWP}, the graph looks linear, which is a result that Honnert et al. (2011) also found for the heat flux close to the surface. Their explanation was that so close to the surface, the function they used to fit the flux partitioning data was no longer independent of z/z_i. Secondly, the point where the resolved and subgrid parts of the total flux are equal for $\overline{w'q'_{\rm t}}$ and $\overline{w'w'}$, shifts to larger $\Delta x_{NWP}/z_i$ when z/z_i increases. At the top of the boundary layer this point shifts back again. This height dependence of the flux partitioning is shown in Fig. 16. The flux partitioning of $\overline{w'\theta'}$ and $\overline{w'\theta'_{\rm v}}$ does not show such a clear trend. For the range $z/z_i = 0.1$-0.4, $\overline{w'\theta'}_{sub}/\overline{w'\theta'}$ reaches values below 0 and above 1. In calculating the ratio of the subgrid flux and the total flux with Eq. (38), we expect that the ratio gives a value between 0 and 1, because the subgrid contribution is a part of the total flux. The appearance of flux partitioning values below 0 and above 1 can be explained by the vertical subgrid flux profiles in Fig. 14(a). There, it can be seen that in the range $z/z_i = 0.1$-0.4, the mean subgrid fluxes $\overline{w'\theta'}_{sub}$ and total flux $\overline{w'\theta'}$ have a different sign or the fluxes do have the same sign, but the subgrid contribution is larger than the resolved flux. In Fig. 14(a), this happens for $\Delta x_{NWP} = 0.1$ km and 0.4 km. Furthermore, it can be seen in Fig. 15 that the ratio $\overline{w'\theta'_{\rm v}}_{sub}/\overline{w'\theta'_{\rm v}}$ drops below 0 around $z/z_i = 0.8$. Fig. 14(c) shows that $\overline{w'\theta'_{\rm v}}_{sub}$ has a different sign than $\overline{w'\theta'_{\rm v}}$ at around $z/z_i = 0.8$. In general, the partition goes outside of the range between 0 and 1 when the vertical profile of the total flux approaches 0. Also, it is visible from Fig. 15 that the flux partitioning of $\overline{w'\theta'}$, $\overline{w'q'_{\rm t}}$ and $\overline{w'\theta'_{\rm v}}$ is not the same. The point where subgrid and resolved contributions to the turbulent flux are equal, is smallest for the buoyancy flux. Thus the turbulent structures of $\theta_{\rm v}$ have the smallest scale, following De Roode et al. (2004). Because $\theta_{\rm v}$ and θ are equal in a dry CBL, the buoyancy flux indicates that the structures of θ would be smaller in a dry CBL than in a CBL with moisture. Finally, the partitioning for heat and moisture fluxes is similar, but not entirely identical. Note that currently the same parametrisatons are used for all scalars in the grey zone. Based on the difference in grey zone transition, it might be necessary to parametrise heat and moisture fluxes separately.

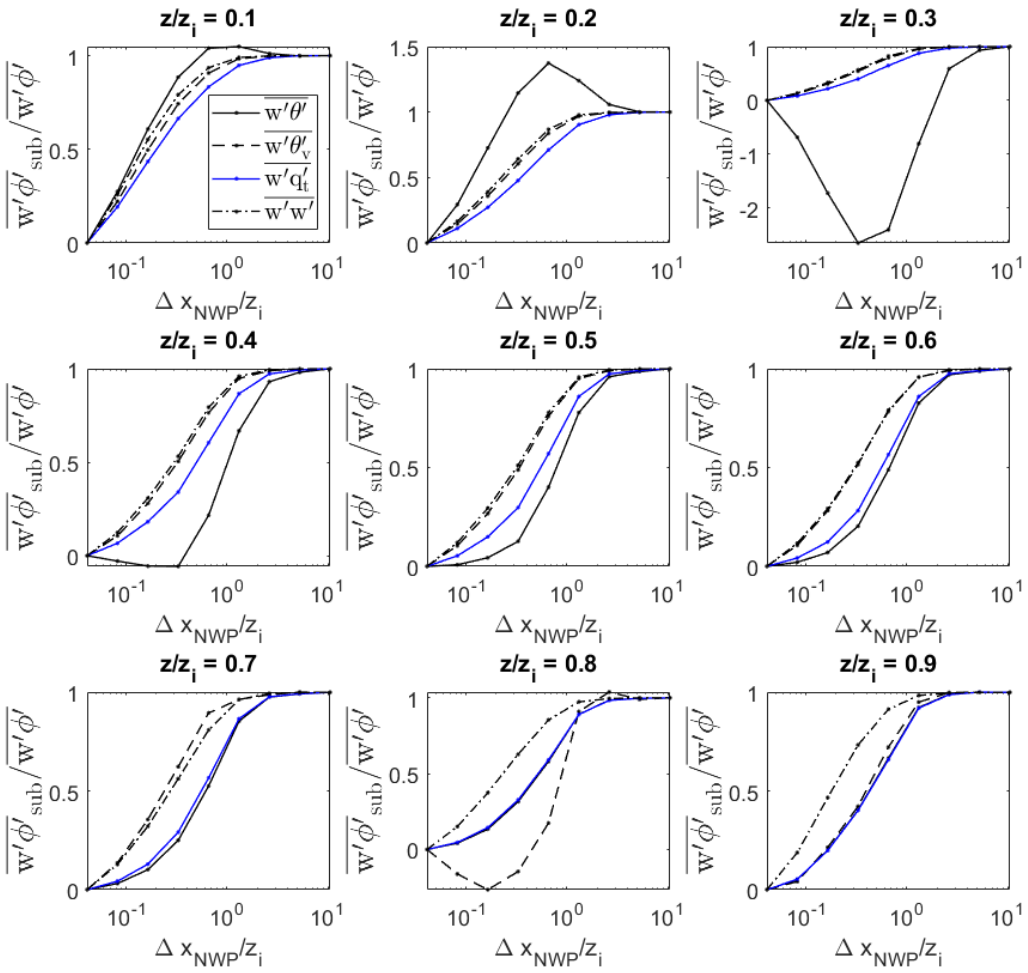

Figure 15: Subgrid flux partitioning of $\overline{w'\theta'}$, $\overline{w'\theta'_{\mathrm{v}}}$, $\overline{w'q'_{\mathrm{t}}}$ and $\overline{w'w'}$ at z/z_i = 0.1-0.9, detemined from instantaneous values at t = 8 h for case CBL.

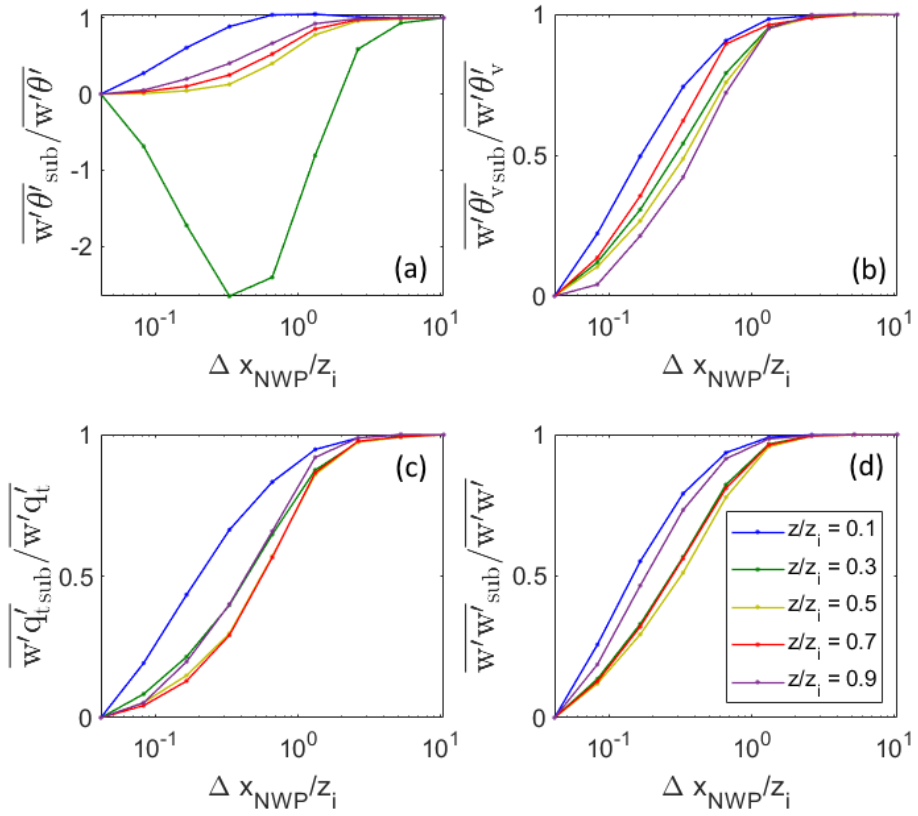

Figure 16: Height dependence of subgrid flux partitioning of (a) $\overline{w'\theta'}$, (b) $\overline{w'\theta'_v}$, (c) $\overline{w'q'_t}$ and (d) $\overline{w'w'}$, determined from instantaneous values at $t = 8$ h for case CBL.

It is clear from Fig. 16 (a) that the flux partitioning varies with height. In characterising the grey zone transition of these fluxes it is interesting to take a closer look at the scale $L_{eq} = \Delta x_{NWP}/z_i$ where the resolved and subgrid fluxes are equal. In Fig. 16, L_{eq} is the point where a graph reaches $\overline{w'\phi'}_{sub}/\overline{w'\phi'}$ = 0.5. L_{eq} is plotted against z/z_i in the boundary layer in Fig. 17. The profile of L_{eq} for the moisture flux slightly increases up until the middle of the boundary layer and then slightly decreases again. This means that the structures in q_t are larger in the middle of the boundary layer than at the surface and the inversion. The profile of L_{eq} for the heat flux gives a completely different picture. A discontinuity occurs for $z/z_i = 0.27$, which is also where the vertical profile of $\overline{w'\theta'}$ switches sign. In a similar plot by Honnert et al. (2011) L_{eq} jumps to a higher value for a z/z_i of about 0.8. This is also the height at which the potential temperature flux switches sign in their simulation case. In both our case and the case of Honnert et al. (2011), the jump to high L_{eq} is caused by the phenomenon that the subgrid and total fluxes have a different sign around the z/z_i where the flux profiles cross zero. There, the partitioning goes to negative values first and then gets to $\overline{w'\theta'}_{sub}/\overline{w'\theta'} = 0.5$ at a much higher Δx_{NWP} than it would otherwise (see Fig. 16(a)). Because of the discontinuity, any conclusion about the size of the structures of θ cannot be drawn.

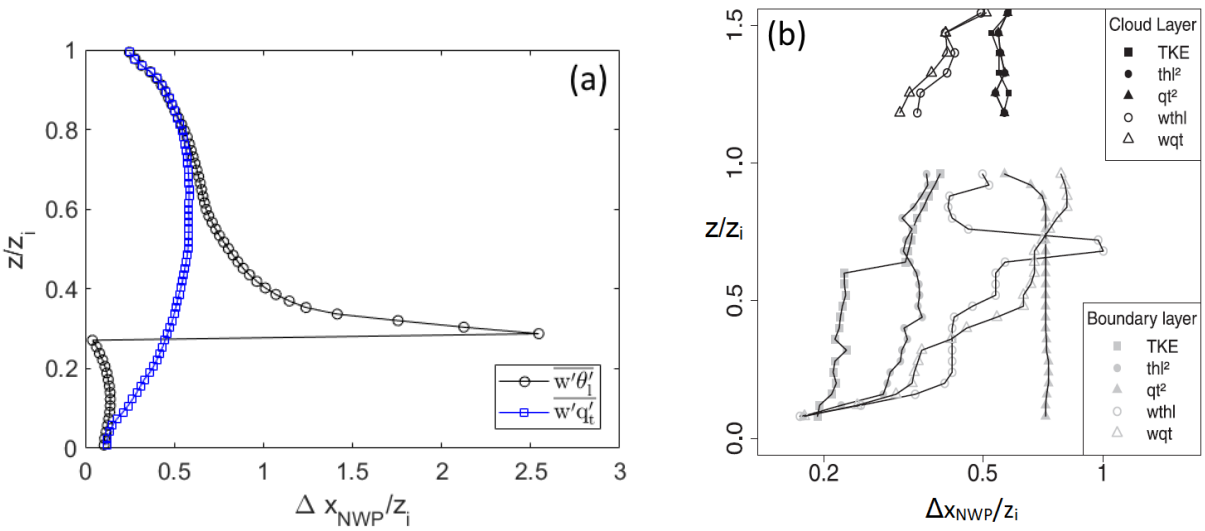

Figure 17: Height profiles of the $\Delta x_{NWP}/z_i$ for which resolved and subgrid contributions to the total flux are equal. The results for fluxes $\overline{w'\theta'}$ and $\overline{w'q'_t}$ are given for case CBL in (a), and the similar figure from Honnert et al. (2011) that depicts these profiles for the TKE, variances of θ and q_t and heat and moisture fluxes, is given in (b).

All in all, the vertical fluxes can be diagnosed well by using the coarse-graining process. The transition from entirely resolved turbulent fluxes to entirely subgrid fluxes can be clearly seen in the pixel plots, flux partitioning and vertical subgrid flux profiles. In chapter 4.2 the results for horizontal and vertical fluxes will be compared.

4.2 Horizontal flux behaviour

4.2.1 Height dependency of slab-averaged horizontal fluxes

In the following, the horizontal fluxes from our analysis will be studied and compared to the vertical fluxes. First, the height profiles of the total horizontal heat, moisture and buoyancy fluxes are given for case CBL and case $\mathrm{CBL_{ws}}$ in Fig. 18. The total fluxes are the LES resolved fluxes, following Eq. (36). The horizontal fluxes have distinctly different height profiles than the vertical fluxes, of which the LES resolved and subgrid fluxes were given in Fig. 9. Let us first focus on case CBL, which has little wind shear (Fig. 18(a)). The flux height profiles for $\overline{u'\theta'}$, $\overline{u'q'_t}$ and $\overline{u'\theta'_v}$ switch sign multiple times in the profile. The horizontal fluxes are the largest at the surface and especially at the top of the boundary layer. At the inversion the horizontal fluxes have the same order of magnitude as the vertical fluxes at their extremes. The horizontal fluxes are large at the top of the boundary layer, because the inversion causes large fluctuations of temperature and humidity. The horizontal heat and buoyancy fluxes in the entrainment zone are positive and the horizontal moisture fluxes are negative. In time, the horizontal fluxes in the entrainment zone become smaller for heat and buoyancy and larger (more negative) for moisture. At the bottom of the boundary layer the increase in horizontal flux magnitude is caused by the surface boundary conditions. In the middle of the the boundary layer, the horizontal fluxes are significantly smaller than at the surface and in the entrainment zone. In the bulk of the boundary layer, the height profile of the horizontal fluxes for all scalars changes over time. The magnitude of the horizontal fluxes does not clearly increase or decrease over time. The total horizontal heat flux in the middle of the boundary layer is about two orders of magnitude smaller than the vertical heat and moisture flux. For the total horizontal moisture and buoyancy flux the difference is smaller, about one order of magnitude. This shows that the slab-averaged horizontal fluxes are of significant magnitude in case CBL, even though they are smaller than the slab-averaged vertical fluxes.

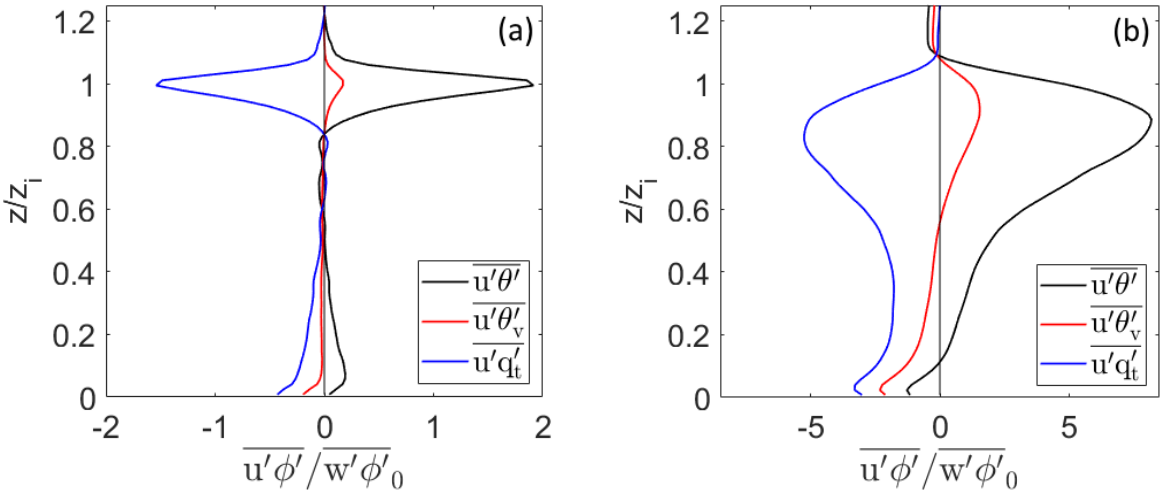

Figure 18: Slab-averaged horizontal total flux profiles for heat, moisture and buoyancy, determined from instantaneous values at $t = 8$ h. The results for case CBL are given in (a) and those for case $\mathrm{CBL_{ws}}$ are given in (b). The horizontal fluxes have been normalised with the surface values for the vertical fluxes, indicated as $\overline{w'\phi'}_0$.

Now we consider case $\mathrm{CBL_{ws}}$ in Fig. 18(b). In case $\mathrm{CBL_{ws}}$, the wind shear increases the momentum flux $\overline{u'w'}$ greatly with respect to case CBL. The increase in momentum flux also makes the horizontal fluxes larger. It is immediately clear that the wind shear has increased the horizontal fluxes drastically. The peaks at the surface and at the inversion, that were visible in the profiles for case CBL, have broadened and penetrated into the bulk of the boundary layer. The inversion is located at about the same height as for case CBL. Over time the horizontal subgrid fluxes for case $\mathrm{CBL_{ws}}$ tend to become slightly smaller in the bulk of the boundary layer and larger at the surface. The magnitude of the horizontal fluxes for case $\mathrm{CBL_{ws}}$ is of the same order as the magnitude of the vertical fluxes in both simulations. In fact, the maximum values of the horizontal fluxes are between twice and four times as large as the maximum values for the vertical.

4.2.2 Scale dependency of horizontal subgrid fluxes

Previously we have seen the height dependency of the total horizontal fluxes and compared it to the vertical fluxes. When we now look at the subgrid fluxes, we can study how the height profiles differ for different Δx_{NWP}. The vertical profiles of the horizontal subgrid fluxes $\overline{u'\theta'}_{sub}$, $\overline{u'q'_t}_{sub}$ and $\overline{u'\theta'_v}_{sub}$, defined as in Eq. (38), are given in Fig. 19 for case CBL and in Fig. 20 for case CBL_{ws}.

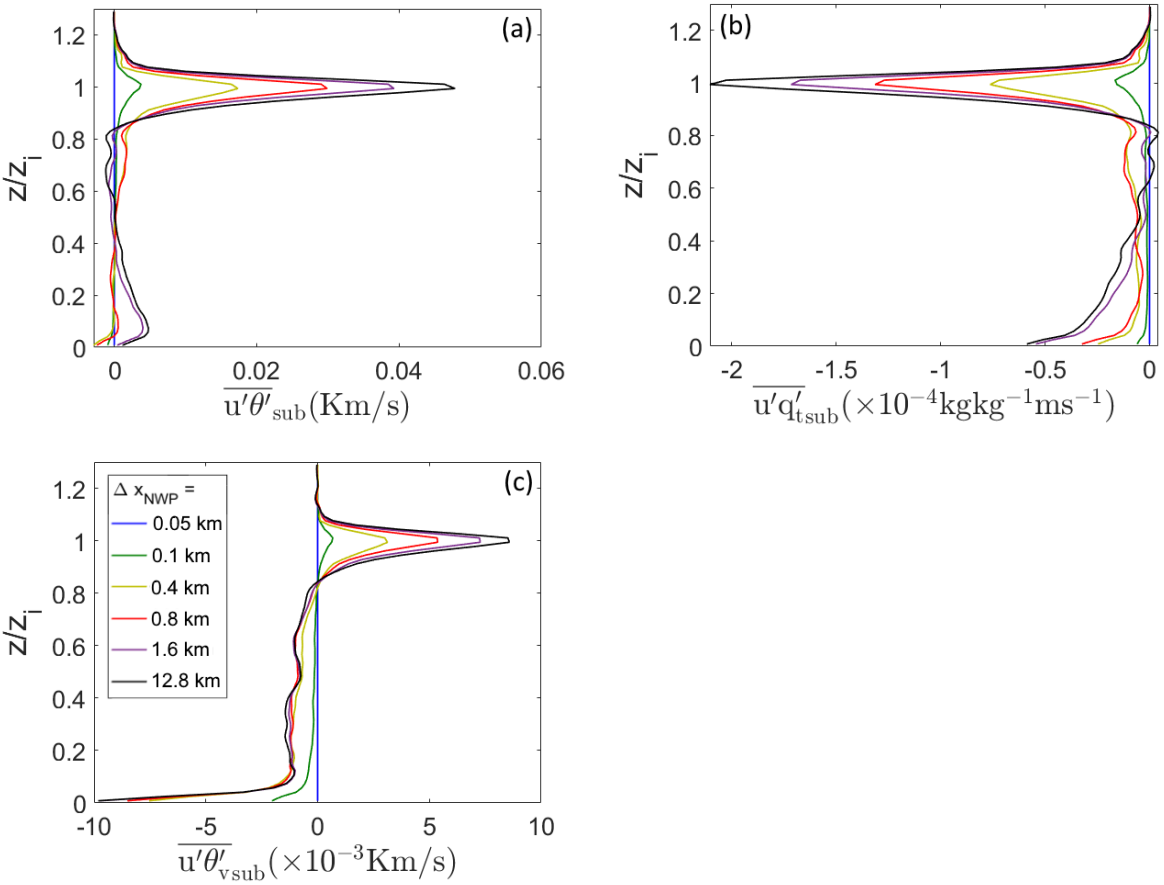

Figure 19: Slab-averaged horizontal subgrid flux profiles for (a) heat, (b) moisture and (c) buoyancy for different Δx_{NWP}, detemined from instantaneous values at $t = 8$ h in case CBL.

In Fig. 19, it can be seen that for case CBL, at the surface and the entrainment zone, the height profiles follow the shape of the total flux (black line) and the magnitude of the horizontal subgrid fluxes decreases steadily for smaller Δx_{NWP}. In the bulk of the boundary layer, the horizontal subgrid flux magnitude does not decrease so clearly. Although the horizontal subgrid fluxes tend to have smaller magnitudes as Δx_{NWP} decreases, there are heights at which the horizontal subgrid fluxes increase in magnitude with respect to the horizontal subgrid fluxes at larger Δx_{NWP}.

In case CBL_{ws}, shown in Fig. 20, the height profiles of horizontal subgrid fluxes follow the shape of the height profile of the total flux (black line) throughout the entire boundary layer. The magnitude of the horizontal subgrid fluxes clearly decreases for smaller Δx_{NWP}. In contrast with case CBL, case CBL_{ws} does not have certain heights in the bulk of the boundary layer where the horizontal subgrid fluxes increase in magnitude relative to the horizontal subgrid fluxes at a larger Δx_{NWP}.

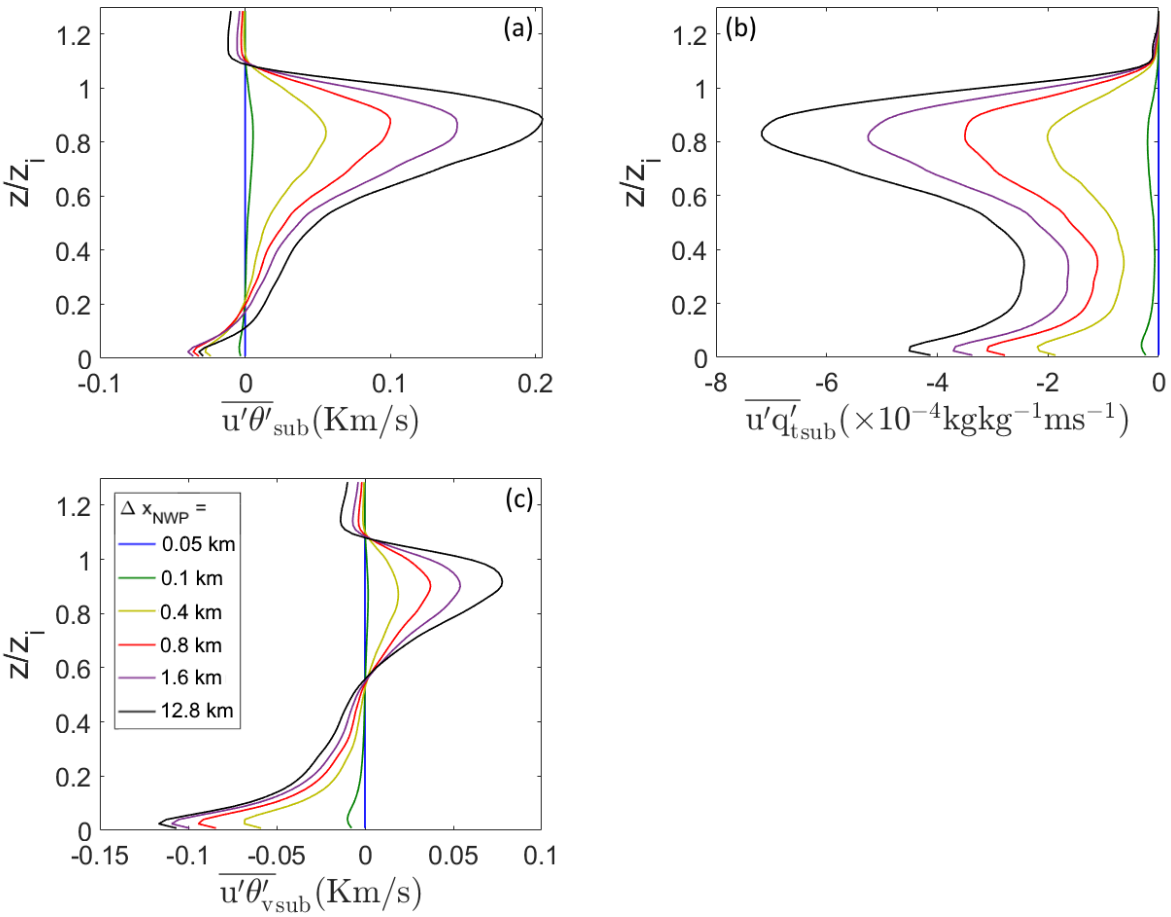

Figure 20: Slab-averaged vertical subgrid flux profiles for (a) heat, (b) moisture and (c) buoyancy for different Δx_{NWP}, determined from instantaneous values at $t = 8$ h in case CBL$_{\text{ws}}$.

Although the height profiles of the slab-averaged horizontal subgrid fluxes give a good impression of their behaviour across the boundary layer, we would like to study the scale dependency of the horizontal fluxes in more detail. To this end, we consider the horizontal fluxes at $z/z_i = 0.5$ for different Δx_{NWP}. As for the vertical fluxes, the scale dependency of the horizontal fluxes can be visualised in pixel plots. In Fig. 21 the horizontal resolved and subgrid heat flux in case CBL are given for different Δx_{NWP}. There we can see that the horizontal resolved flux has a similar behaviour as the vertical flux. The subgrid flux is small at first and then begins to show some structures, just like in the vertical. However, as Δx_{NWP} approaches the domain size, the subgrid flux reduces to a much smaller value than for the vertical. For case CBL$_{\text{ws}}$, shown in Fig. 22, it appears that the subgrid flux does go to significant positive value at $\Delta x_{NWP} = L_x$.

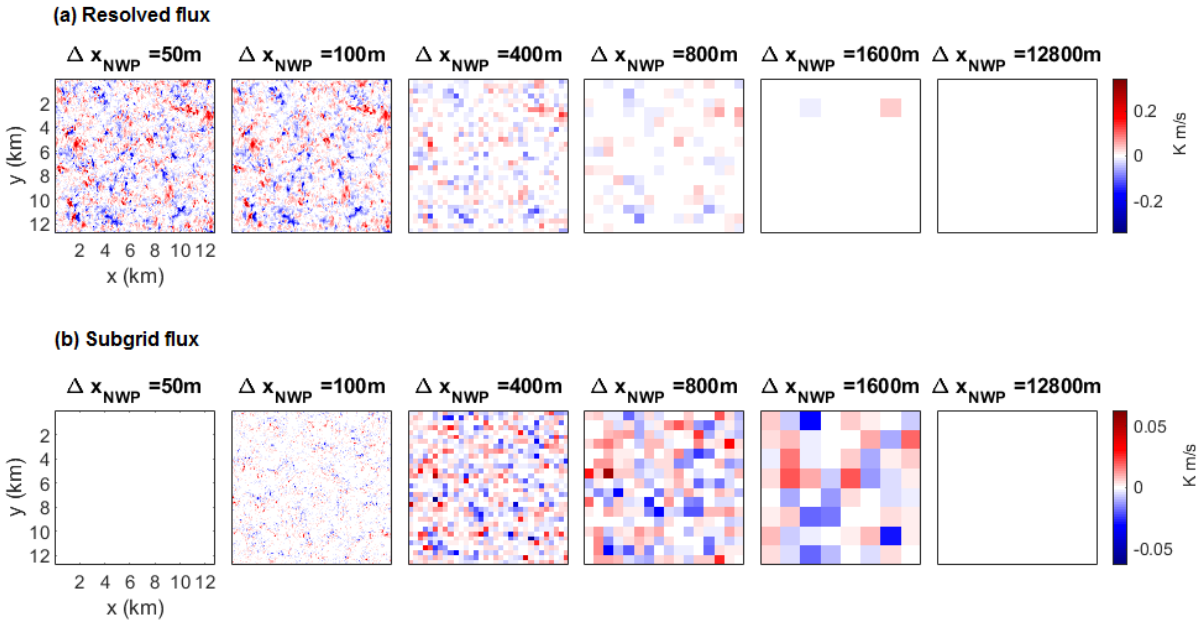

Figure 21: (a) Pixel plots of the horizontal resolved heat flux $u''\theta''_{res} = (\langle u \rangle - \overline{u})(\langle \theta \rangle - \overline{\theta})$ and (b) pixel plots of the horizontal subgrid heat flux $\langle u''\theta'' \rangle$, determined from instantaneous values at t = 8 h, z/z_i = 0.5 and case CBL.

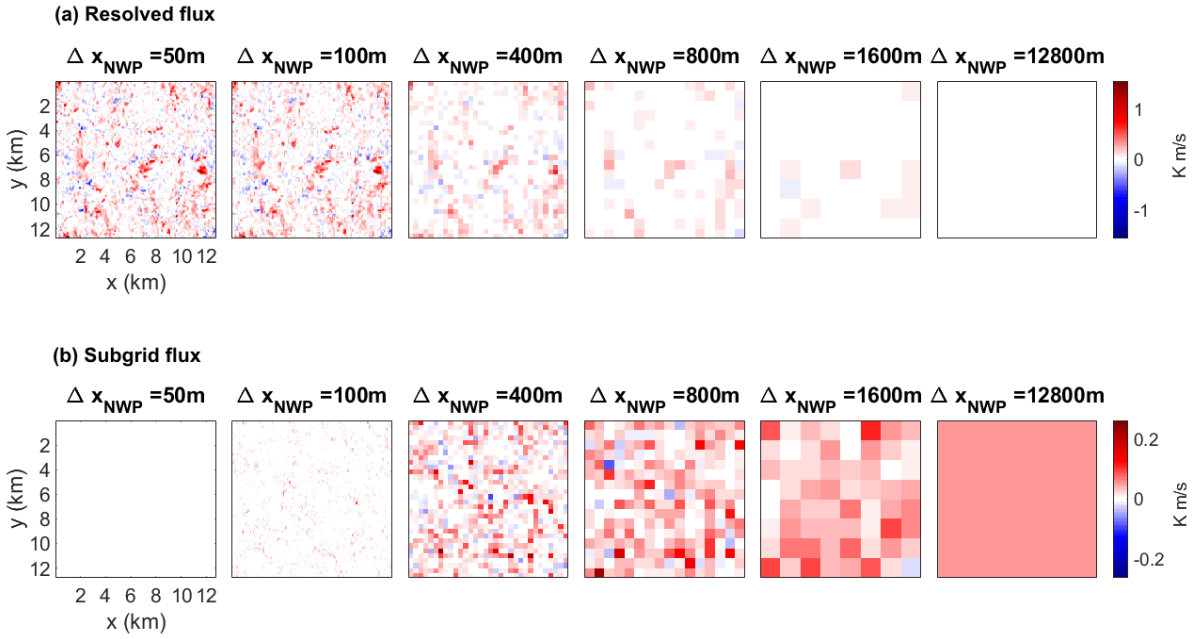

Figure 22: (a) Pixel plots of the horizontal resolved heat flux $u''\theta''_{res} = (\langle u \rangle - \overline{u})(\langle \theta \rangle - \overline{\theta})$ and (b) pixel plots of the horizontal subgrid heat flux $\langle u''\theta'' \rangle$, determined from instantaneous values at t = 8 h, z/z_i = 0.5 and case CBL_{ws}.

The probability density functions of $\langle u''\theta'' \rangle$ for case CBL, shown in Fig. 23(a), reflect the pixel plots. The PDF for the horizontal fluxes is narrow for small Δx_{NWP} and then spreads out. In contrast with the vertical flux distribution, which converged to -0.02 Kms^{-1}, the PDF for the horizontal subgrid fluxes becomes a narrow peak around a very small value of 1.4×10^{-4} Kms^{-1} at $\Delta x_{NWP} = L_x$. Indeed, the slab-averaged values of the horizontal heat flux are two orders of magnitude smaller than the vertical

heat fluxes, which was already visible in Fig. 19. However, the width of the PDFs is almost the same for horizontal and vertical fluxes. The PDFs for case CBL_{ws} are given in Fig. 23(b). In case CBL_{ws}, the PDF becomes a narrow peak at $\Delta x_{NWP} = L_x$ around a value of 0.05 Kms^{-1}, which is two orders of magnitude larger than the value for case CBL. This proves that the higher wind speed in case CBL_{ws} siqnificantly increases the magnitude of the horizontal subgrid fluxes.

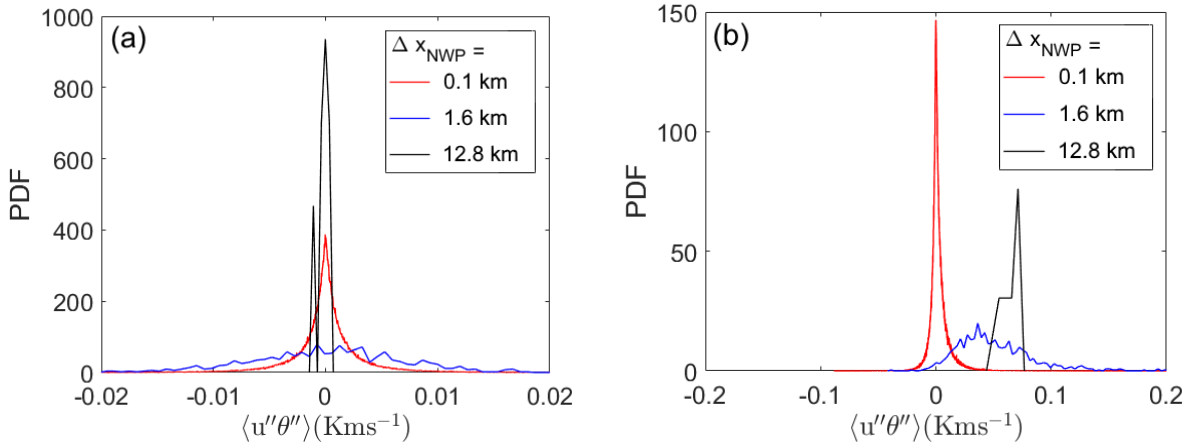

Figure 23: Distribution of the horizontal heat fluxes $\langle u''\theta''\rangle$ for $z/z_i = 0.5$. In (a) the fluxes are given for case CBL and in (b) they are given for case CBL_{ws}. The distributions are created from multiple LES fields sampled every 5 minutes between $t = 7$ h and $t = 8$ h. The horizontal axis has been limited from -0.02 to 0.02 Kms^{-1} in (a) and from -0.2 to 0.2 Kms^{-1} in (b).

Now that the height and scale dependencies of the horizontal subgrid fluxes have been discussed, we compare the vertical and horizontal subgrid fluxes more explicitly. The magnitudes of vertical and horizontal subgrid fluxes for heat and moisture in case CBL are compared in Fig. 24(a). The vertical subgrid fluxes show a steady increase across the scales, which levels off at $\Delta x_{NWP} = 3.2$ km. The magnitude of horizontal subgrid fluxes overall becomes larger for increasing grid sizes, but not as rapidly as the magnitude of the vertical subgrid fluxes. At some grid sizes, the magnitude of the horizontal fluxes decreases relative to magnitude at a smaller grid size. At small Δx_{NWP}, the horizontal subgrid fluxes are only half an order of magnitude smaller than the vertical subgrid fluxes. As Δx_{NWP} increases, the magnitude difference increases to two orders of magnitude. In case CBL_{ws}, shown in Fig. 24(b), a more rapid increase in magnitude can be seen for the horizontal subgrid fluxes. The scale dependency of the magnitude of the horizontal subgrid fluxes for case CBL_{ws} is comparable to that of the vertical subgrid fluxes. The magnitude of the horizontal subgrid fluxes even becomes larger than the magnitude of the vertical subgrid fluxes at large grid sizes. The vertical subgrid fluxes are also slightly larger in case CBL_{ws} than in case CBL. The slight increase in vertical subgrid flux magnitude and the large increase in horizontal subgrid flux magnitude compared to case CBL, are a direct result from the high momentum flux in CBL_{ws}. The results in Fig. 24 are in line with the height profiles of the slab-averaged vertical and horizontal subgrid fluxes seen earlier in in Figs. 14, 19 and 20. The height profiles also show that the magnitude of the vertical fluxes increases as Δx_{NWP} becomes larger, consistent with Fig. 24(a). The magnitude of the horizontal fluxes in case CBL does not increase very clearly in Fig. 24(a), which is also visible in the height profiles in Fig. 19. In the height profiles we can also see that for case CBL the vertical subgrid fluxes are up to two orders of magnitude larger than the horizontal subgrid fluxes. At $z/z_i = 0.5$, the horizontal and vertical subgrid fluxes have about the same magnitude in case CBL_{ws}, which is also apparent in Fig. 24. That the magnitude of the horizontal subgrid fluxes in case CBL_{ws} increases rapidly with grid size can also be seen in Fig. 20. All in all, the height profiles and the plots of the slab-averaged fluxes against different grid sizes are consistent.

According to Eq. (31), the subgrid fluxes in an NWP might be predicted following a down-gradient diffusion approach. In order to compare the magnitude of the subgrid fluxes with that of the scalar gradients, the slab-average of the absolute value of the potential temperature gradient is given in Fig. 25 for the horizontal and vertical direction in case CBL and case $\mathrm{CBL_{ws}}$. It makes sense to take the absolute value here, because the values of the potential temperature gradient span several orders of magnitude and should be plotted on a logarithmic scale for clarity.

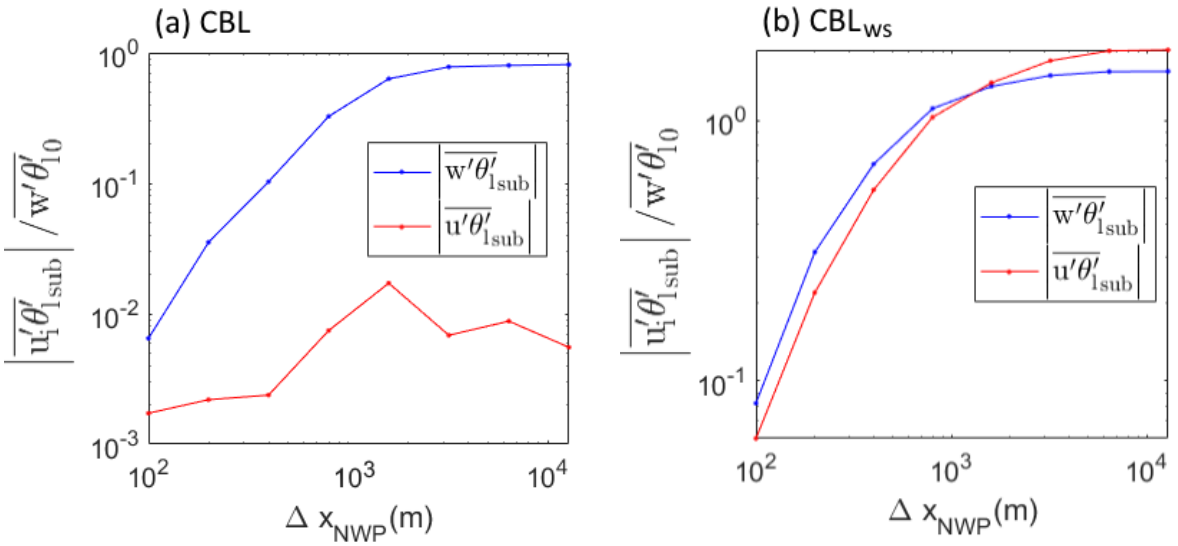

Figure 24: The absolute value of the vertical and horizontal heat fluxes normalised by the vertical surface heat flux for different Δx_{NWP}, determined from instantaneous values at $t = 8$ h, for $z/z_i = 0.5$. The surface values are indicated with a subscript 0. The results for case CBL are given in (a), those for case $\mathrm{CBL_{ws}}$ in (b).

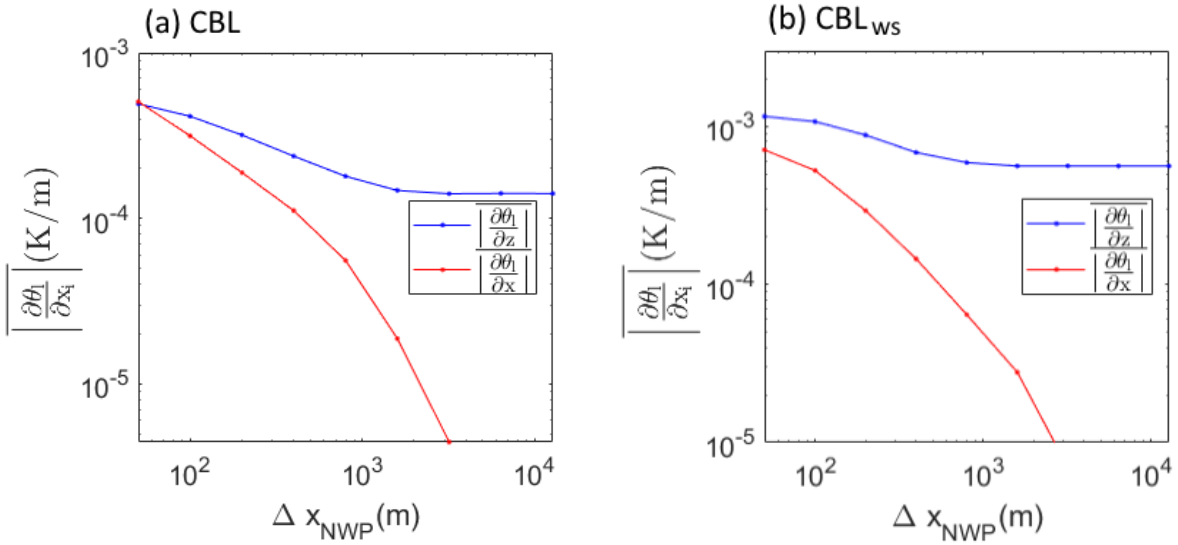

Figure 25: The slab-average of the absolute values for the vertical and horizontal potential temperature gradients for different Δx_{NWP}, determined from instantaneous values at $t = 8$ h, for $z/z_i = 0.5$. The results for case CBL are given in (a), those for case $\mathrm{CBL_{ws}}$ in (b). At $\Delta x_{NWP} = \frac{1}{2}L_x$ and $\Delta x_{NWP} = L_x$, the horizontal potential temperature gradients are zero and therefore cannot be shown on the vertical logarithmic axis.

For case CBL, the vertical temperature gradient drops off slightly and goes to an asymptotic value, whereas for case CBL_{ws}, the vertical temperature gradient is almost constant for every value of Δx_{NWP}. As the vertical potential temperature gradient stays within the same order of magnitude for all Δx_{NWP}, and the vertical subgrid fluxes increase with grid size in both cases (see Fig. 24), the eddy diffusivity for vertical transport K_z must increase with grid size as well. In Fig. 25, we can also see that the magnitude of the horizontal potential temperature gradient decreases rapidly with grid size for both cases. The magnitude of the horizontal potential temperature gradient decreases, while the magnitude of the horizontal heat fluxes increases. From these results it cannot be found directly with Eq. (31) how K_x depends on the grid size. Also, for $\Delta x_{NWP} = 6.4$ km and $\Delta x_{NWP} = 12.8$ km, the horizontal potential temperature gradient is zero, while the horizontal subgrid fluxes are nonzero. Therefore the eddy diffusivity K_x will be undefined at those grid sizes. We will analyse the grid dependency of K_z and K_x in further detail in chapter 4.3.

Kurowski and Teixeira (2018) give a similar plot to Fig. 24, where they obtain the vertical and horizontal heat fluxes from their LES parametrisation in simulations that use a range of resolutions from $\Delta x = 0.05$ km to $\Delta x = 100$ km (see Fig. 26). They conclude that the vertical subgrid fluxes slowly increase with grid size and reach an asymptotic value at $\Delta x = 10$ km. Albeit that the asymptotic value is reached at a lower grid size, we find the same behaviour for the vertical subgrid fluxes in our results. In Fig. 26, it can also be seen that the horizontal subgrid fluxes slightly decrease and then rapidly decrease beyond $\Delta x = 4$ km. In addition, they show that the potential temperature gradient decreases with increasing grid size and the eddy diffusivity K increases. They assume, as do we, that the horizontal flux, potential temperature gradient and eddy diffusivity are interconnected via Eq. (31). The eddy diffusivity they use is the same for the vertical and horizontal direction. Kurowski and Teixeira (2018) argue that up until $\Delta x_{NWP} = 4$ km, the increase in eddy diffusivity balances out the decrease in potential temperature gradient, keeping the horizontal heat fluxes at a stable level. However, when the eddy diffusivity levels off, the temperature gradient still decreases, so the horizontal fluxes collapse to very low values. In our results, we do not see such a steep magnitude drop at large Δx_{NWP}. In fact, the horizontal subgrid fluxes show an increase in magnitude as the grid sizes become larger. It can be concluded that our diagnosis of the horizontal subgrid fluxes produces profoundly different results than the parametrisation of Kurowski and Teixeira (2018).

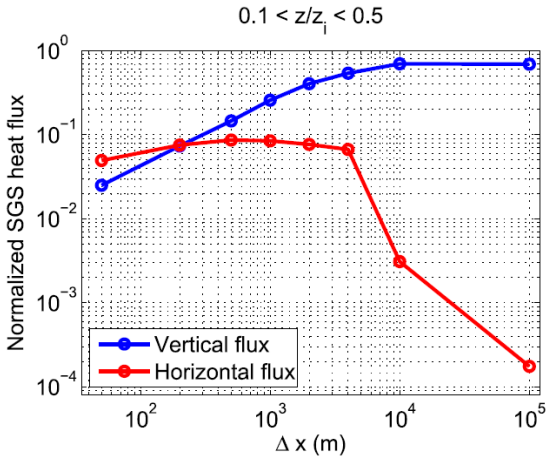

Figure 26: Slab-averaged subgrid vertical and horizontal fluxes for $z/z_i = 0.1$-0.5 normalised by the surface heat flux. Image copied from Kurowski and Teixeira (2018).

4.2.3 Comparison of flux divergences and their calculation methods

To assess the contribution of horizontal subgrid fluxes to the tendencies of the mean in NWP models, we look at the horizontal flux divergences. The horizontal flux divergences have been obtained using three different calculation methods, specified in chapter 3.3. Depending on the calculation method used, the horizontal flux divergences are denoted by $\langle\frac{\partial u''\theta''}{\partial x}\rangle_{adv}$, $\langle\frac{\partial u''\theta''}{\partial x}\rangle_{dir}$ or $\frac{\partial\langle u''\theta''\rangle}{\partial x}$. For convenience we summarise the calculation methods in the following. Firstly, the flux divergence can be found from the advection term in the scalar equation and is then denoted by $\langle\frac{\partial u''\theta''}{\partial x}\rangle_{adv}$. The flux divergence $\langle\frac{\partial u''\theta''}{\partial x}\rangle_{adv}$ plus an additional term B can be diagnosed from $\langle\frac{\partial u\phi}{\partial x}\rangle$ and $\frac{\partial\langle u\rangle\langle\phi\rangle}{\partial x}$,

$$\left\langle\frac{\partial u''\phi''}{\partial x}\right\rangle_{adv}+B=\left\langle\frac{\partial u\phi}{\partial x}\right\rangle-\frac{\partial\langle u\rangle\langle\phi\rangle}{\partial x}. \tag{39}$$

Secondly, $\langle\frac{\partial u''\phi''}{\partial x}\rangle_{dir}$ is calculated with the values of $u''\phi''$ located at the borders of the subdomain as,

$$\left\langle\frac{\partial u''\phi''}{\partial x}\right\rangle_{dir\,I,J}=\frac{1}{n_y}\sum_{j=1}^{n_y}\frac{u''\phi''_{n_x+\frac{1}{2},j}-u''\phi''_{\frac{1}{2},j}}{\Delta x_{NWP}}. \tag{40}$$

Finally, the flux divergence $\frac{\partial\langle u''\phi''\rangle}{\partial x}$ is found by taking the gradient of the subgrid flux in a subdomain,

$$\frac{\partial\langle u''\phi''\rangle}{\partial x}_{I,J}=\frac{\langle u''\phi''\rangle_{I+1,J}-\langle u''\phi''\rangle_{I-1,J}}{2\Delta x_{NWP}}. \tag{41}$$

In Fig. 27, the PDFs for the horizontal flux divergences $\langle\frac{\partial u''\theta''}{\partial x}\rangle_{adv}$, $\langle\frac{\partial u''\theta''}{\partial x}\rangle_{dir}$ and $\frac{\partial\langle u''\phi''\rangle}{\partial x}$ are given for Δx_{NWP} = 0.1 km, 0.8 km and 3.2 km in case CBL.

A similarity across the PDFs of the flux divergences in both simulation cases is that they centre around zero, due to the following reason. Because $\overline{u'\phi'}(0)=\overline{u'\phi'}(L_x)$, the subgrid flux divergence converges to zero for any simulation and calculation method. There are also differences between the PDFs. It is evident that the PDFs for $\langle\frac{\partial u''\theta''}{\partial x}\rangle_{adv}+B$ are much wider than those of the other two methods. In fact, the PDFs have a width that is three orders of magnitude larger than the distribution widths for the vertical flux divergence. If we compare the distribution widths of the flux divergence $\langle\frac{\partial u''\theta''}{\partial x}\rangle_{adv}+B$ with those of $\langle\frac{\partial u''\theta''}{\partial x}\rangle_{dir}$ specifically, we observe that the former are about four orders of magnitude larger than the latter. If we disregard numerical differences, $\langle\frac{\partial u''\theta''}{\partial x}\rangle_{dir}$ shows what the distribution of $\langle\frac{\partial u''\theta''}{\partial x}\rangle_{adv}$ would look like without the additional terms B. The large width difference between the distributions suggests that the contributions B are large (see Eq. (39) and appendix B). The terms B are even larger than the flux divergence $\langle\frac{\partial u''\theta''}{\partial x}\rangle_{adv}$ itself. Therefore we can conclude that $\langle\frac{\partial u''\theta''}{\partial x}\rangle_{adv}$ cannot be diagnosed directly from $\langle\frac{\partial u\phi}{\partial x}\rangle$ and $\frac{\partial\langle u\rangle\langle\phi\rangle}{\partial x}$, which we know from the LES field.

The flux divergence $\langle\frac{\partial u''\theta''}{\partial x}\rangle$ can be diagnosed both from the advection term in the scalar equation and directly from the LES field. However, the subgrid transport term in the NWP budget equation is written with the averaging operator inside of the differential operator, as $\frac{\partial\langle u''\theta''\rangle}{\partial x}$ (see Eq. (14)). The widths of the distributions for the flux divergence $\frac{\partial\langle u''\theta''\rangle}{\partial x}$ are about a factor of 3 smaller than those of $\langle\frac{\partial u''\theta''}{\partial x}\rangle_{dir}$. The smaller magnitude of the $\frac{\partial\langle u''\theta''\rangle}{\partial x}$ flux divergences indicates that the term $B_{u''\phi''}$ in Eq. (29) is significant. In addition, numerical differences play a role in the difference between $\frac{\partial\langle u''\theta''\rangle}{\partial x}$ and $\langle\frac{\partial u''\theta''}{\partial x}\rangle_{dir}$. For example, for Δx_{NWP} = 6.4 km and 12.8 km the value of $\frac{\partial\langle u''\theta''\rangle}{\partial x}$ is always zero, whereas $\langle\frac{\partial u''\theta''}{\partial x}\rangle_{dir}$ is zero for Δx_{NWP} = 12.8 km, but nonzero for Δx_{NWP} = 6.4 km. The grid sizes where the flux divergence is zero follow directly from how both variants of the flux divergences were defined in Eq. (40) and Eq. (41), respectively. Moreover, $\frac{\partial\langle u''\theta''\rangle}{\partial x}$ uses the data points from coarse-grained grid boxes at $I-1$ and $I+1$ (see Eq. (41)). It is not based on the local fluctuations in the grid box at I, where we want to know the flux divergence. This makes $\frac{\partial\langle u''\theta''\rangle}{\partial x}$ less representative of the local subgrid transport.

All in all, when we attempt to diagnose the flux divergence $\langle\frac{\partial u''\theta''}{\partial x}\rangle$ from the advection term, we find the flux divergence plus additional terms B of significant magnitude. Instead the flux divergence can be found directly from the LES field. This flux divergence, $\langle\frac{\partial u''\theta''}{\partial x}\rangle_{dir}$, is the term that appears when we derive the scalar equation for NWP models (see chapter 3.3). However, the subgrid transport term in the scalar

equation is currently written as $\frac{\partial \langle u''\theta'' \rangle}{\partial x}$. We have seen that taking the differential operator inside the averaging operator to obtain $\frac{\partial \langle u''\theta'' \rangle}{\partial x}$ from $\langle \frac{\partial u''\theta''}{\partial x} \rangle$ introduces a nonzero boundary term $B_{u''\phi''}$. So, the flux divergence as it is currently written in the NWP budget equation, underestimates the contribution of the subgrid transport to the tendencies of the mean.

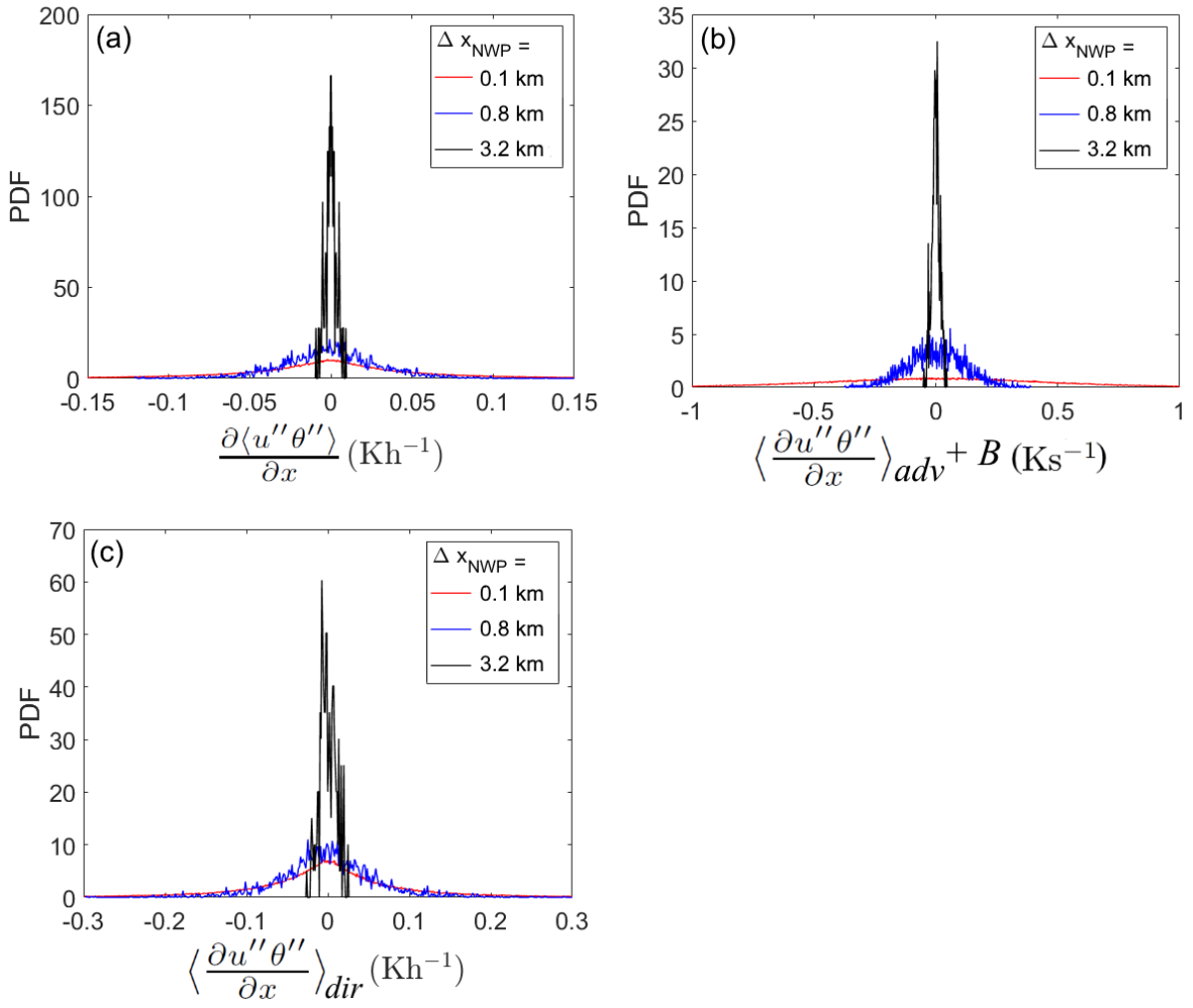

Figure 27: Distributions of flux divergences (a) $\frac{\partial \langle u''\theta'' \rangle}{\partial x}$, (b) $\langle \frac{\partial u''\phi''}{\partial x} \rangle_{adv} + B$ and (c) $\langle \frac{\partial u''\theta''}{\partial x} \rangle_{dir}$, for z/z_i = 0.5 and case CBL. The distributions are created from multiple LES fields sampled every 5 minutes between t = 7 h and t = 8 h. The x-axis has been limited to values between -0.15 and 0.15 Kh^{-1} for (a), -1 and 1 Ks^{-1} for (b) and -0.3 and 0.3 Kh^{-1} for (c), to exclude the values that are almost zero.

In addition to the comparison of the three methods of obtaining the flux divergence, we can also use it to compare the contribution of vertical and horizontal fluxes to the tendencies of the mean. If we just consider the vertical and horizontal transport in the form of $\langle \frac{\partial w''\theta''}{\partial z} \rangle$ and $\langle \frac{\partial u''\theta''}{\partial x} \rangle$ in Fig. 13(b) and Fig. 27(c-d), respectively, we can conclude that the widths of the distributions for vertical transport are only a factor of 2 larger than the widths of the distributions for horizontal transport. The distributions having a comparable width suggests that vertical and horizontal subgrid transport contribute similarly to the tendency of the mean in the grey zone. This is an important result, because it shows that, in the grey zone, we have to take horizontal subgrid transport into account. Although the NWP models that operate at grid sizes beyond grey zone resolutions neglect horizontal subgrid transport, it is clear that this assumption is no longer valid within the grey zone.

4.3 K-diffusion analysis

In the following, the scale and directional dependency of the eddy diffusivity is explored in further detail. We focus on the eddy diffusivity for moisture K_{q_t}, because its values are positive everywhere in the boundary layer. $\langle K_{q_t} \rangle$ is the eddy diffusivity in a particular subdomain. It is defined for both the vertical and horizontal direction according to Eq. (34), as the ratio of the subgrid flux and the scalar gradient in that subdomain. For a particular $\Delta x_{NWP}/z_i$, each subdomain will have a separate vertical K-profile. This is illustrated in Fig. 28, where the vertical profiles of the eddy diffusivity are given for the entire domain and for the four subdomains that remain at $\Delta x_{NWP} = 6.4$ km. The slab-averaged eddy diffusivity $\overline{K}_{q_t,z}$ over the entire slab gives a strictly positive vertical profile in the boundary layer (see Fig. 28(a)). In Fig. 28(b) it can be seen that the four subdomains at $\Delta x_{NWP} = 6.4$ km each have a different vertical profile.

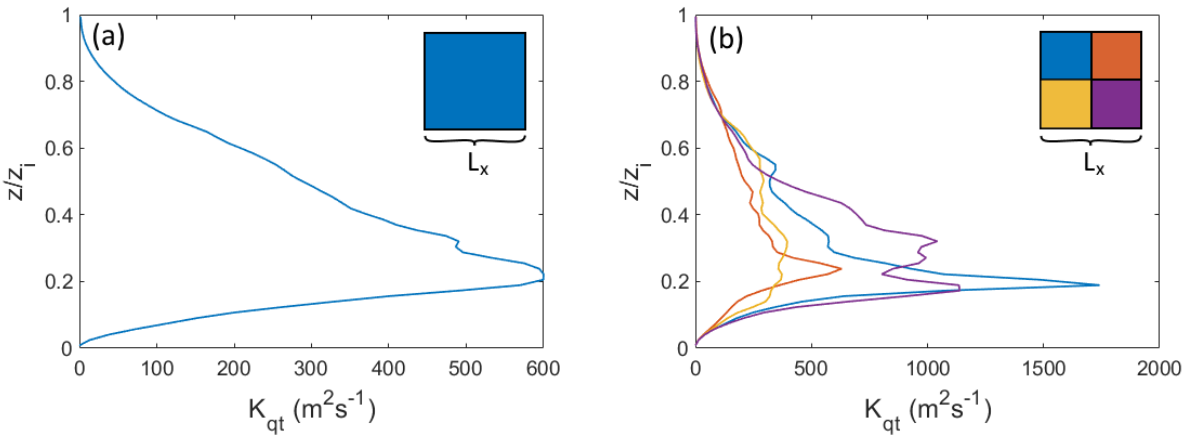

Figure 28: Vertical profile for $\overline{K}_{q_t,z}$ (a) and vertical profiles of $\langle K \rangle_{q_t,z}$ for the four subdomains at Δx_{NWP} = 6.4 km (b), determined from instantaneous values at $t = 8$ h, for case CBL.

To probe the scale dependency of K, a representative average is calculated for different Δx_{NWP} at z/z_i = 0.1, 0.5 and 0.7. The K-value representing the average for a certain Δx_{NWP} at a particular height is obtained using two different methods. Using an arithmetic mean is not practical here, because there exist very large outlier values in the sample that make the mean biased toward those values. To keep the outliers from affecting the result too much, the median of the distribution of subdomain K-values, K_{median}, can be used to represent the average instead. Alternatively, $\langle K_{q_t} \rangle$ can be found by fitting a linear relation through a scatter plot of $\frac{\partial \langle q_t \rangle}{\partial z}$ and $\langle w'' q_t'' \rangle$. A linear least squares fitting procedure is used to fit a line through the origin. The slope of the fitted graph indicates the value of K_{fit}. K_{median} and K_{fit} are plotted against Δx_{NWP}. If the methods yield similar results, it is an indication of the robustness of the results. According to Eq. (32), it is expected that K will be lower for smaller Δx_{NWP}, because the mixing length l is known to decrease with smaller Δx_{NWP} (Efstathiou and Beare (2015)). The analysis can be extended to θ, as well as the x-direction.

In Fig. 29(a) the vertical eddy diffusivity $K_{q_t,z}$ is plotted against $\Delta x_{NWP}/z_i$. Both methods show that $K_{q_t,z}$ increases rapidly at small Δx_{NWP} and then reaches an asymptotic value at $\Delta x_{NWP} = 3.2$ km. Note that K_{fit} lacks the last data point at $\Delta x_{NWP} = L_x$, because there were too few data points to do a meaningful fit. Besides this, the two methods of obtaining $K_{q_t,z}$ give results that are in agreement. Also, we can determine the eddy diffusivity for the entire slab directly with Eq. (34), by dividing the slab-averaged vertical subgrid flux by the vertical gradient of the slab-averaged q_t. This eddy diffusivity is also shown in Fig. 29(a). The value of K_{median} at $\Delta x_{NWP} = L_x$ is similar to the actual value determined directly via Eq. (34). This means that the median represents the slab-average of the eddy diffusivity suitably.

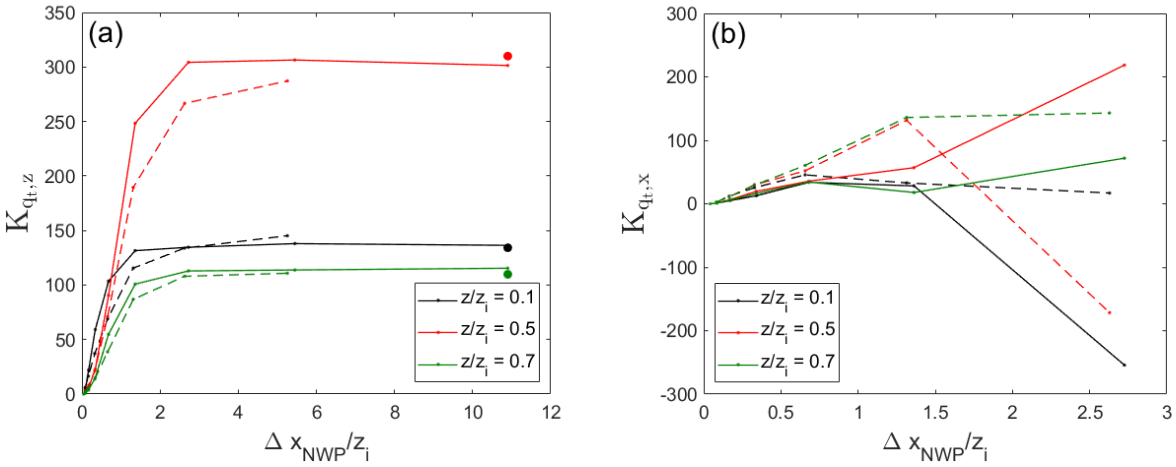

Figure 29: $K_{q_t,z}$ (a) and $K_{q_t,x}$ (b) from the median (continuous lines) and from linear fitting (dashed lines) plotted against $\Delta x_{NWP}/z_i$ at $z/z_i = 0.1$, 0.5 and 0.7 for case CBL. The results for the median are obtained from multiple LES fields sampled every 5 minutes between $t = 7$ h and $t = 8$ h. The fit was done with the instantaneous values for $t = 8$ h. In (a) the values of K for the entire domain determined directly with Eq. (34) are shown as dots at $\Delta x_{NWP} = L_x$.

The horizontal eddy diffusivity $K_{q_t,x}$ is plotted against Δx_{NWP} for case CBL in Fig. 29(b). The behaviour of $K_{\theta,x}$ and $K_{q_t,x}$ is similar, so $K_{\theta,x}$ is not shown here. For the horizontal, K_{median} and K_{fit} look very different. For small Δx_{NWP}, it seems that $K_{q_t,x}$ increases almost linearly for both the medians and the fitted values. The values are significant, suggesting that we do need to take the horizontal subgrid flux into account in the grey zone. At larger $\Delta x_{NWP}/z_i$ the median and fitted values start to diverge for $z/z_i = 0.5$ and 0.7. At $z/z_i = 0.1$ both methods are in agreement until before the value at $\Delta x_{NWP}/z_i = 2.7$, which corresponds with $\Delta x_{NWP} = 3.2$ km. The values at $\Delta x_{NWP}/z_i = 2.7$ are quite unreliable, because they are based on few data points. For Δx_{NWP} larger than 3.2 km, the horizontal potential temperature gradients are zero, while the horizontal subgrid fluxes are nonzero. Therefore the eddy diffusivity K obtained via Eq. (34) is meaningless at these grid sizes. The results for $K_{q_t,x}$ in case CBL_{ws} show increasingly negative values for larger grid sizes. These negative values suggest some form of counter-gradient transport, which does not follow the widely used down-gradient diffusion approach (Eq. (31)). From Fig. 29, it also appears that the eddy diffusivity is different for vertical and horizontal transport. Note that currently an isotropic eddy diffusivity is used in Smagorinsky-type subgrid models. The comparison of K_z and K_x shows that their scale dependency is not the same. Note that we can only compare K_z and K_x at grid sizes smaller than $\Delta x_{NWP} = 3.2$ km, because at larger grid sizes the eddy diffusivity cannot be defined using Eq. (34). Nevertheless, for grid sizes up until 3.2 km, it can be concluded that there is a need for an anisotropic model for the eddy diffusivity. The eddy diffusivity for horizontal transport K_x and for vertical transport K_z have to be defined separately.

5 Conclusion

Coarse-graining high-resolution LES results makes it possible to diagnose the scale dependency of vertical and horizontal fluxes as well as their divergences that control the temporal changes of the grid box mean values. Both subgrid and resolved fluxes were analysed from the coarse-grained fields. Two LES simulation cases were used in the experiment. The first case, referred to as case CBL, is a CBL case in which the buoyancy flux has a strong contribution from the moisture flux (see De Roode et al. (2004) for details). The second case is a CBL case with strong wind shear and subsidence, called case $\mathrm{CBL_{ws}}$.

First we studied the results for the vertical fluxes, to confirm that the coarse-graining approach yielded results that could be physically understood and were in agreement with existing literature. From our results we found that the vertical turbulent fluxes are entirely resolved at the LES resolution, and are no longer resolved at the onset of the grey zone, at resolutions of around 10 km. Such a transition from resolved to subgrid turbulent fluxes in the grey zone is consistent with flux partitioning shown in Honnert et al. (2011) and Shin and Hong (2013). It was also found that the magnitude of the vertical subgrid fluxes increases with grid size, until it levels off at a 3.2 km grid size. The grid size at which resolved and subgrid contributions to the turbulent flux of a particular quantity are equal, is a measure for the scale of the structures of that quantity. The grid size where resolved and subgrid contributions are equal in this experiment, measured in the middle of the boundary layer, indicated that the turbulent structures for θ_v have a smaller scale than for θ and q_t, which is in agreement with De Roode et al. (2004). Because in a dry boundary layer θ and θ_v are equal, the flux for θ_v also shows that the scale of the structures for θ would be smaller in a dry CBL as compared to the CBL with moisture. Corroborating the result from Honnert et al. (2011), we find that the transition from resolved to subgrid fluxes is different for θ and q_t, which is an indication that they have to be parametrised separately, instead of using the same scalar eddy diffusivity for both quantities.

Horizontal turbulent fluxes, like the vertical fluxes, are no longer resolved at resolutions of about 10 km. In case CBL, we find that below the entrainment zone, the horizontal heat, moisture and buoyancy fluxes are up to two orders of magnitude smaller than the vertical fluxes. However, when we increase the momentum flux by imposing a greater wind shear in case $\mathrm{CBL_{ws}}$, the magnitude of the horizontal heat, moisture and buoyancy fluxes even becomes larger than the magnitude of the vertical fluxes. This shows that the wind shear has a large effect on the horizontal subgrid fluxes. Like the vertical subgrid fluxes, the horizontal subgrid fluxes overall become larger with increasing grid size. In case CBL, the magnitude of the horizontal subgrid fluxes does not increase consistently and sometimes decreases with respect to the magnitude at a smaller grid size. Case $\mathrm{CBL_{ws}}$ does show a steady increase in horizontal subgrid flux magnitude as the grid size increases. Interestingly, Kurowski and Teixeira (2018) found that the subgrid horizontal fluxes decrease with grid size, which is completely opposite to what we conclude from our results. Furthermore, to see how the horizontal subgrid fluxes influence the tendency of the mean quantities in an NWP model, we looked at the horizontal flux divergences. To visualise the flux divergences we plotted their probability distributions. In both case CBL and case $\mathrm{CBL_{ws}}$, the slab-averaged horizontal flux divergences over the entire LES domain will be zero due to periodic boundary conditions. Therefore we focus on the width of the distributions to determine the impact of the horizontal subgrid transport on the tendency of the mean quantities in an NWP model. We also diagnosed the distributions for the vertical flux divergence, which gives this impact for vertical transport. When we compare the vertical and horizontal flux divergences, it is found that the width of the distributions for the vertical and horizontal flux divergences have the same order of magnitude. This means that the vertical and horizontal transport contribute similarly to the tendency of the mean in NWP models. In NWP models with grid sizes beyond grey zone resolutions, the horizontal transport is usually neglected under the assumption of horizontal homogeneity of the turbulent field. However, our findings suggest that this assumption is no longer valid in the grey zone, so horizontal transport has to be taken into account. Also, the effects of the periodic boundary conditions on the flux divergence are not yet known exactly. In future work, a larger LES domain could be simulated to avoid the possible influence of the periodic boundary conditions.

Finally, we diagnose the scale and directional dependency of the eddy diffusivity K, to determine whether or not it is suitable to use a down-gradient diffusion approach in an NWP parametrisation. From the coarse-grained fields we know the vertical and horizontal subgrid fluxes and scalar gradients for a range of grid sizes. K can be determined from the subgrid fluxes and scalar gradients for each grid box at

a particular grid size and height. Using the median of the distribution of all values of K at a particular height, or linearly fitting a relation between the scalar gradients and the subgrid fluxes, both give a meaningful representative for the average of K. The eddy diffusivity for vertical transport increases rapidly and then reaches an asymptotic value for a grid size of 3.2 km. However, the eddy diffusivity for horizontal transport does not show the same scale dependency as for vertical transport. K_x has positive and negative values and does not seem to converge to a single value. Moreover, at grid sizes above 3.2 km, K_x is undefined in this experiment. This is because, at those grid sizes the horizontal scalar gradients are zero, while the horizontal subgrid fluxes are nonzero. At least for the grid sizes below 3.2 km, we can say that K_z and K_x do not have the same scale dependency. Kurowski and Teixeira (2018) also showed the scale dependency of the eddy diffusivity K. However, they used the same eddy diffusivity for the vertical and horizontal direction. Their results are in agreement with our results for the vertical direction, but not for the horizontal direction. The difference in scale dependency between K_z and K_x from our results suggests that an isotropic K, which is used by Kurowski and Teixeira (2018) as well as in DALES itself, is not appropriate in the grey zone. K also appears in the approach that Boutle et al. (2014) use to represent partially resolved turbulence in the grey zone. Their parametrisation relies in part on a Smagorinsky-type model that solves the TKE equation using a down-gradient diffusion approach for the buoyancy flux and wind shear production term. The anisotropy of K that is found in our results should be taken into account in any parametrisation where a down-gradient diffusion approach is used. From our LES results we are able to diagnose the scale dependency of K_z in a down-gradient diffusion approach, which validates the literature. K_z increases with grid size to an asymptotic value. For K_x, we find positive and negative values and the values beyond 3.2 km are undefined. Therefore, further study of the eddy diffusivity for horizontal transport is needed to establish whether it makes sense physically to base parametrisations on it for the grey zone, or if it needs to be abandoned altogether.

The analyses of the vertical subgrid fluxes are largely in agreement with the literature, making the coarse-graining of LES fields a valuable diagnostic tool for vertical subgrid fluxes. For the horizontal subgrid fluxes, there is little other material to compare the results with. In further work, horizontal subgrid fluxes should be diagnosed using different simulation cases and domain sizes. This will further expand our understanding of the behaviour of the horizontal subgrid fluxes in the grey zone.

References

Boutle, I. A., J. E. J. Eyre, and A. P. Lock, 2014: Seamless stratocumulus simulation across the turbulent gray zone. *Monthly Weather Review*, **142**, 1655–1668.

Brown, A. R., S. H. Derbyshire, and P. J. Mason, 1994: Large-eddy simulation of stable atmospheric boundary layers with a revised stochastic subgrid model. *Quarterly Journal of the Royal Meteorological Society*, **120**, 1485–1512.

De Roode, S. R., P. G. Duynkerke, and H. J. J. Jonker, 2004: Large eddy simulation: How large is large enough? *Journal of Atmospheric Sciences*, **61**, 403–421.

De Roode, S. R., H. J. J. Jonker, B. J. H. van de Wiel, V. Vertregt, and V. Perrin, 2017: A diagnosis of excessive mixing in Smagorinsky subfilter-scale turbulent kinetic energy models. *Journal of Atmospheric Sciences*, **74**, 1495–1511.

De Roode, S. R., and Coauthors, 2019: Turbulent transport in the gray zone: A large eddy model intercomparison study of the CONSTRAIN cold air outbreak case. *Journal of Advances in Modeling Earth Systems*, **11**, 597–623.

Deardorff, J. W., 1973: Three-dimensional numerical modeling of the planetary boundary layer. *Workshop on Micrometeorology*, D. A. Haugen, Ed., American Meteorological Society, 271-311.

Deardorff, J. W., 1980: Stratocumulus-capped mixed layers derived from a three-dimensional model. *Boundary-layer Meteorology*, **18**, 495–527.

Efstathiou, G. A., and R. J. Beare, 2015: Quantifying and improving sub-grid diffusion in the boundary-layer grey zone. *Quarterly Journal of the Royal Meteorological Society*, **141**, 3006–3017.

Heus, T., and Coauthors, 2010: Formulation of the Dutch Atmospheric Large-Eddy Simulation (DALES) and overview of its applications. *Geoscientific Model Development*, **3**, 415–444.

Honnert, R., V. Masson, and F. Couvreux, 2011: A diagnostic for evaluating the representation of turbulence in atmospheric models at the kilometric scale. *Journal of Atmospheric Sciences*, **68**, 3112–3131.

Kurowski, M. J., and J. Teixeira, 2018: A scale-adaptive turbulent kinetic energy closure for the dry convective boundary layer. *Journal of Atmospheric Sciences*, **75**, 675–690.

Leonard, A., 1974: Energy cascade in large-eddy simulations of turbulent fluid flows. *Advances in Geophysics*, **18A**, 237–248.

Mason, P. J., and D. J. Thomson, 1992: Stochastic backscatter in large-eddy simulations of boundary layers. *Journal of Fluid Mechanics*, **242**, 51–78.

Nieuwstadt, F. T. M., B. J. Boersma, and J. Westerweel, 2016: *Turbulence*. Springer.

Nieuwstadt, F. T. M., P. J. Mason, C.-H. Moeng, and U. Schumann, 1993: Large-eddy simulation of the convective boundary layer: A comparison of four computer codes. *Turbulent Shear Flows 8*, F. Durst, R. Friedrich, B. Launder, F. Schmidt, U. Schumann, and J. Whitelaw, Eds., Springer, 343-367, doi: 10.1007/978-3-642-77674-8_24.

Shin, H. H., and S. Hong, 2013: Analysis of resolved and parametrised vertical transports in convective boundary layers at gray-zone resolutions. *Journal of Atmospheric Sciences*, **70**, 3248–3261.

Simon, J. S., B. Zhou, J. D. Mirocha, and F. K. Chow, 2019: Explicit filtering and reconstruction to reduce grid dependence in convective boundary layer simulations using WRF-LES. *Monthly Weather Review*, doi:10.1175/MWR-D-18-0205.1.

Wyngaard, J. C., 2004: Toward numerical modeling in the "terra incognita". *Journal of Atmospheric Sciences*, **61**, 1816–1826.

Appendix

A - Self-similar coarse-graining

This coarse-graining method generates a self-similar grid with a series of interpolations (see figure 30). For each coarse-graining step a staggered grid is obtained, with the velocities at the face centres and the scalar quantities in the centre of the grid box. First the scalar quantities are averaged with Eq. (18) as described in chapter 3.3. The velocities can also be averaged using Eq. (18). The resulting average velocities are located between the face and the centre of the grid box, while the scalar averages are located at the grid box centres. The coarse-grained grid is now not structured in the same way as the original grid and additional steps have to be taken to make the grid self-similar. The approach is illustrated in Fig. 30. Firstly, the two distinct average velocities are found with Eq. (18) for two overlapping sets of four points. These are $\langle u \rangle_{I-\frac{1}{4},J}$ and $\langle u \rangle_{I-\frac{3}{4},J}$. For coarse-graining order n the average velocities are found with Eqs. (42),

$$\begin{aligned} \langle u \rangle_{I-\frac{1}{4},J,n} &= \frac{1}{n_x n_y} \sum_{i=n_x(I-1)+1}^{n_x I} \sum_{j=n_y(J-1)+1}^{n_y J} u_{i-\frac{1}{2},j} \\ \langle u \rangle_{I-\frac{3}{4},J,n} &= \frac{1}{n_x n_y} \sum_{i=n_x(I-1)+1}^{n_x I} \sum_{j=n_y(J-1)+1}^{n_y J} u_{i-1\frac{1}{2},j} \end{aligned}, \tag{42}$$

where $n_x = n_y = 2^n$. The grid created by the previous coarse-graining order forms the basis for the new grid. In every coarse-graining step, the indices of the previous grid are i and j and the indices of the new grid are I and J. So after each step I and J turn into i and j. In order to create the self-similar average velocity $\langle u \rangle_{I+\frac{1}{2},J}$ at the side of the grid box, an interpolation is required,

$$\langle u \rangle_{I-\frac{1}{2},J,n} = \frac{\langle u \rangle_{I-\frac{1}{4},J,n} + \langle u \rangle_{I-\frac{3}{4},J,n}}{2}. \tag{43}$$

A self-similar grid can be obtained in this manner for every coarse-graining order n. This coarse-graining method can be applied in the y-direction for the other horizontal velocity v, to find $\langle v \rangle$. The average vertical velocity $\langle w \rangle$ requires a less complicated calculation. The average velocity at every height is calculated using Eq. (18). Then the average velocities $\langle w \rangle$ are located at the bottom face of every grid box. The self-similar grid method was ultimately abandoned in favour of the method implemented in the research, because the latter proved much easier to implement and gives a more direct approach to the coarse-graining process. The self-similar grid method uses so many interpolations that it is difficult to say if it provides an accurate representation of an output grid with a larger grid size.

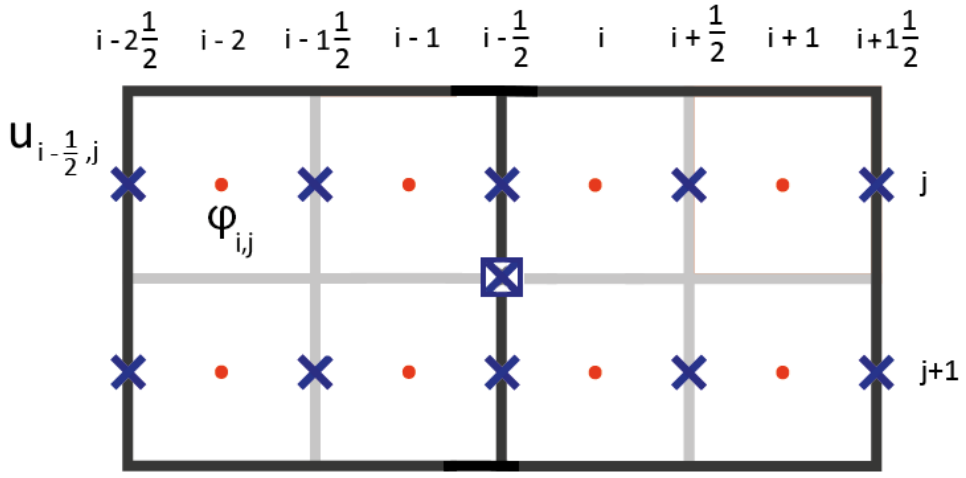

(a) Before averaging u is present at the half levels

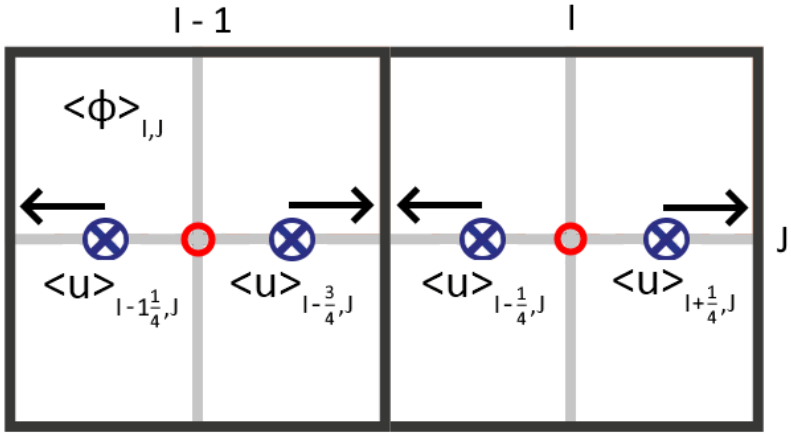

(b) After averaging <u> is located at the quarter levels of the new grid

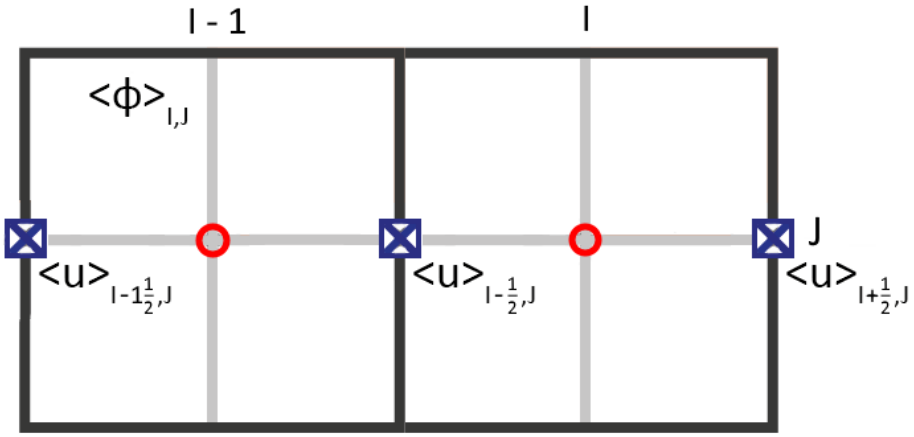

(c) Interpolating the averaged velocities <u> we obtain <u> at the half levels of the new grid

Figure 30: The self-similar coarse-graining method. Red dots denote the positions of scalars ϕ and the blue crosses denote the positions of velocities u. The average $\langle\phi\rangle$ is depicted as a red circle. Intermediate averages of u at the quarter levels are shown as blue circled crosses and the final average is shown as a blue boxed cross.

B - Derivation of the subdomain-averaged advection and flux divergences

Our objective is to diagnose the flux divergence $\langle \frac{\partial u'' \phi''}{\partial x} \rangle$ from the advection term $\langle \frac{\partial u \phi}{\partial x} \rangle$ in the scalar equation. Ignoring molecular dissipation we can write for the scalar equation,

$$\frac{\partial \phi}{\partial t} = -u\frac{\partial \phi}{\partial x} - v\frac{\partial \phi}{\partial y} - w\frac{\partial \phi}{\partial z}. \tag{44}$$

Using the continuity equation Eq. (44) can be rewritten as,

$$\frac{\partial \phi}{\partial t} = -\frac{\partial u\phi}{\partial x} - \frac{\partial v\phi}{\partial y} - \frac{\partial w\phi}{\partial z}. \tag{45}$$

If we apply the subdomain averaging operator $\langle . \rangle$ to Eq. (45), we obtain,

$$\Big\langle \frac{\partial \phi}{\partial t} \Big\rangle = -\Big\langle \frac{\partial u\phi}{\partial x} \Big\rangle - \Big\langle \frac{\partial v\phi}{\partial y} \Big\rangle - \Big\langle \frac{\partial w\phi}{\partial z} \Big\rangle. \tag{46}$$

With an approach similar to Reynolds averaging, the advection term averaged over the subdomain $\langle \frac{\partial u\phi}{\partial x} \rangle$ can be expanded by replacing u and ϕ according to Eq. (19),

$$\Big\langle \frac{\partial u\phi}{\partial x} \Big\rangle = \Big\langle \frac{\partial}{\partial x}(\langle u \rangle + u'')(\langle \phi \rangle + \phi'') \Big\rangle = \Big\langle \frac{\partial \langle u \rangle \langle \phi \rangle}{\partial x} \Big\rangle + \Big\langle \frac{\partial \langle u \rangle \phi''}{\partial x} \Big\rangle + \Big\langle \frac{\partial u'' \langle \phi \rangle}{\partial x} \Big\rangle + \Big\langle \frac{\partial u'' \phi''}{\partial x} \Big\rangle. \tag{47}$$

To further simplify Eq. (47), we want to bring the averaging operator inside the differential operator for the first three terms. In the following, we will use f to represent the flux-like quantities $\langle u \rangle \langle \phi \rangle$, $\langle u \rangle \phi''$ or $u'' \langle \phi \rangle$ that appear in Eq. (47). For the sake of the this derivation, we consider the sudomain-averaging in 2D (the x and y-direction). According to Leonard (1974), the subdomain averaging as in Eq. (18) can be written as a convolution of the function f with a function G_0 that defines the filtering method,

$$\langle f \rangle = \iint G_0(x - x', y - y') f(x', y') dx' dy'. \tag{48}$$

In this case we use a simple square filter given by,

$$G_0(x - x', y - y') = \begin{cases} \frac{1}{\Delta x_{NWP}^2}, & \text{for } 0 \leq x - x' \leq \Delta x_{NWP},\ 0 \leq y - y' \leq \Delta x_{NWP} \\ 0, & \text{otherwise} \end{cases}. \tag{49}$$

Note that we assume here that f is continuous. The quantities that are represented by f come from the LES fields of u and ϕ, which are of course discrete. For convenience the function $G_0(x - x', y - y')$ is split into two identical functions for the x- and y-direction,

$$G(x - x', y - y') = G(x - x')G(y - y'), \tag{50}$$

with,

$$G(x - x') = \begin{cases} \frac{1}{\Delta x_{NWP}}, & \text{for } 0 \leq x - x' \leq \Delta x_{NWP} \\ 0, & \text{otherwise} \end{cases}. \tag{51}$$

Now we can write $\langle \frac{\partial f}{\partial x} \rangle$ as,

$$\Big\langle \frac{\partial f}{\partial x} \Big\rangle = \int G(y - y') \int G(x - x') \frac{\partial f(x', y')}{\partial x'} dx' dy'. \tag{52}$$

Integration by parts gives,

$$\Big\langle \frac{\partial f}{\partial x} \Big\rangle = \int G(y - y') \left(\Big[f(x', y') G(x - x') \Big] - \int f(x', y') \frac{\partial G(x - x')}{\partial x'} dx' \right) dy'. \tag{53}$$

It can be shown that $\frac{\partial G(x-x')}{\partial x'} = -\frac{\partial G(x-x')}{\partial x}$. If we apply this to Eq. (53), the sign is flipped before the second integral and G is differentiated to x instead of x',

$$\Big\langle \frac{\partial f}{\partial x} \Big\rangle = \int G(y - y') \left(\Big[f(x', y') G(x - x') \Big] + \int f(x', y') \frac{\partial G(x - x')}{\partial x} dx' \right) dy'. \tag{54}$$

Now $\frac{\partial}{\partial x}$ can be taken outside the second integral. Splitting the equation into two integral terms we obtain,

$$\left\langle \frac{\partial f}{\partial x} \right\rangle = \int G(y-y') \Big[f(x',y') G(x-x') \Big] dy' + \frac{\partial}{\partial x} \iint G(y-y') G(x-x') f(x',y') dx' dy'. \tag{55}$$

The second term can be rewritten with Eq. (48), and becomes equal to $\frac{\partial \langle f \rangle}{\partial x}$. In addition, $G(x-x')$ and $G(y-y')$ are substituted in Eq. (55) according Eq. (51). The functions G limit f to the interval between $x - \Delta x_{NWP}$ and x and they give the bounds of the integral over y',

$$\left\langle \frac{\partial f}{\partial x} \right\rangle = \frac{1}{\Delta x_{NWP}^2} \int_{y-\Delta x_{NWP}}^{y} \Big[f_{\Delta x_{NWP}}(x',y') \Big] dy' + \frac{\partial \langle f \rangle}{\partial x}, \tag{56}$$

where $f_{\Delta x_{NWP}}$ is defined as the function f limited to the interval between $x - \Delta x_{NWP}$ and x,

$$f_{\Delta x_{NWP}}(x',y') = \begin{cases} f(x',y'), & \text{for } x - \Delta x_{NWP} \leq x' \leq x \\ 0, & \text{otherwise} \end{cases}. \tag{57}$$

The positions x and y determine for which grid box the average is calculated. Note that the quantities represented by f have discontinuities at multiples of Δx_{NWP}, which are the grid box borders, so it is not trivial to find f there. Summarised, when we take the averaging operator inside the differential operator an additional term appears,

$$\left\langle \frac{\partial f}{\partial x} \right\rangle = B_f + \frac{\partial \langle f \rangle}{\partial x}. \tag{58}$$

Here we denote the additional term that arises when converting $\langle \frac{\partial f}{\partial x} \rangle$ to $\frac{\partial \langle f \rangle}{\partial x}$ by B_f. The additional term B_f is thus given by,

$$B_f = \frac{1}{\Delta x_{NWP}^2} \int_{y-\Delta x_{NWP}}^{y} f_{\Delta x_{NWP}} dy \tag{59}$$

With Eqs. (58) and (59), which give the additional terms that appear when we take the averaging operator inside the differential operator, we can rewrite Eq. (47) as,

$$\begin{aligned} \left\langle \frac{\partial u\phi}{\partial x} \right\rangle = & \frac{\partial \langle \langle u \rangle \langle \phi \rangle \rangle}{\partial x} + \int_{y-\Delta x_{NWP}}^{y} \langle u \rangle \langle \phi \rangle_{\Delta x_{NWP}} dy \\ & + \frac{\partial \langle \langle u \rangle \phi'' \rangle}{\partial x} + \int_{y-\Delta x_{NWP}}^{y} \langle u \rangle \phi''_{\Delta x_{NWP}} dy \\ & + \frac{\partial \langle u'' \langle \phi \rangle \rangle}{\partial x} + \int_{y-\Delta x_{NWP}}^{y} u'' \langle \phi \rangle_{\Delta x_{NWP}} dy \\ & + \left\langle \frac{\partial u'' \phi''}{\partial x} \right\rangle. \end{aligned} \tag{60}$$

The average of a fluctation is zero, so the cross-terms drop out. Their additional terms remain, however. Removing the cross-terms and summarising the additional terms as B, we can write,

$$\left\langle \frac{\partial u\phi}{\partial x} \right\rangle = \frac{\partial \langle u \rangle \langle \phi \rangle}{\partial x} + \left\langle \frac{\partial u'' \phi''}{\partial x} \right\rangle + B. \tag{61}$$

Here B is a summation of the terms $B_{\langle u \rangle \langle \phi \rangle}$, $B_{\langle u \rangle \phi''}$ and $B_{u'' \langle \phi \rangle}$ (see the notation B_f in Eq. (59)). Individually, the additional terms are given by the integral over y of the function $f_{\Delta x_{NWP}}$ following Eq. (59),

$$
\begin{aligned}
B &= B_{\langle u\rangle\langle\phi\rangle} + B_{\langle u\rangle\phi''} + B_{u''\langle\phi\rangle} \\
&= \int_{y-\Delta x_{NWP}}^{y} \langle u\rangle\langle\phi\rangle_{\Delta x_{NWP}} dy \\
&\quad + \int_{y-\Delta x_{NWP}}^{y} \langle u\rangle\phi''_{\Delta x_{NWP}} dy \\
&\quad + \int_{y-\Delta x_{NWP}}^{y} u''\langle\phi\rangle)_{\Delta x_{NWP}} dy.
\end{aligned}
\tag{62}
$$

Note that it is not straightforward to obtain B because of the discontinuities on the grid box borders of the quantities $\langle u\rangle\langle\phi\rangle$, $\langle u\rangle\phi''$ and $u''\langle\phi\rangle$. In the study, B is estimated by comparing the $\langle\frac{\partial u''\phi''}{\partial x}\rangle + B$ found from the difference between $\langle\frac{\partial u\phi}{\partial x}\rangle$ and $\frac{\partial\langle u\rangle\langle\phi\rangle}{\partial x}$, with the $\langle\frac{\partial u''\phi''}{\partial x}\rangle_{dir}$ obtained directly from the LES field.

Furthermore, Eqs. (58) and (59) also describe the term $B_{u''\phi''}$ that appears when $\langle\frac{\partial u''\phi''}{\partial x}\rangle$ becomes $\frac{\partial\langle u''\phi''\rangle}{\partial x}$. The former follows from the scalar equation and is not equal to the latter, which is the form currently used in the NWP budget equation (see Eq. (14)). We repeat Eq. (29) where $B_{u''\phi''}$ appears,

$$
\left\langle\frac{\partial u''\phi''}{\partial x}\right\rangle = \frac{\partial\langle u''\phi''\rangle}{\partial x} + B_{u''\phi''}. \tag{63}
$$

Generally $B_{u''\phi''}$ is nonzero due to a discontinuity at the boundary. Seeing as $\frac{\partial\langle u''\phi''\rangle}{\partial x}$ is the form of the flux divergence used in the NWP budget equation and $\langle\frac{\partial u''\phi''}{\partial x}\rangle$ is the form that we derived from the coarse-graining the scalar equation (see Eq. (47)), it is important to diagnose $B_{u''\phi''}$. Only if $B_{u''\phi''}$ is small, it is justified to use $\frac{\partial\langle u''\phi''\rangle}{\partial x}$ instead of $\langle\frac{\partial u''\phi''}{\partial x}\rangle$ in the NWP budget equation.

Taking the averaging operator inside the differential operator does not generate an additional term B_f for derivatives along the z-direction. This is because the averaging operator and the differential operator work along different directions. The averaging operator takes the average in the x- and y-direction according to Eq. (18). The differential operator $\frac{\partial}{\partial z}$ is directed along the z-direction. Because the operators act along different directions, extra terms do not appear.